Supporting Information

Therapeutic Coordination Polymers: Tailoring Drug Release through Metal-Ligand Interactions

Table of Contents

General Comments

Single-crystal X-ray diffraction data were collected on a Bruker D8 Venture diffractometer, with either a Cu microfocus X-ray source with 2D Montel multilayer optics or a Mo-sealed X-ray tube with a curved graphite monochromator. All crystals were collected at 170 K, except for **ZnDiclo6**, which was collected at 298 K due to extreme smearing of reflections at colder temperatures.

Powder X-ray diffractograms were collected with one of two XRD systems from PROTO Manufacturing; a PROTO AXRD Benchtop Powder Diffraction System using Cu $K\alpha_{avg}$ radiation with a DECTRIS Mythen silicon strip detector with an angular 2Θ range of 4-50°, a step size of 0.015°, and a dwell time of 2 seconds or a PROTO High-throughput Laboratory Powder Diffractometer (LPD-HT) equipped with a Cu $K\alpha_{avg}$ microfocus X-ray source, 2D Montel focusing optics, and a DECTRIS 1M Eiger2 area detector with angular coverage of 45^{o} 2Θ.

Thermogravimetric analysis of materials was performed on a TA Instrument (TGA 5500). All samples were held isothermally for 10 minutes under N_2 before being heated at a rate of 10 °C per minute until a maximum temperature of 600 °C was reached.

IR spectra were collected using a Bruker Alpha FT-IR spectrometer equipped with a platinum single-reflection diamond ATR module. A PerkinElmer 2400 Series II Elemental Analyzer was used for elemental analysis. All UV-Vis samples were measured on an Agilent 8453 spectrophotometer.

Drug dissolution and intrinsic dissolution rates were obtained using a Varian VK 7000 pharmaceutical dissolution instrument connected to a VK8000 autosampler and peristaltic pump. Dissolution studies were performed using United States Pharmacopeia (USP) apparatus one (paddles) at 100 rpm. Approximately 30 mg of each TCP was compacted into a disc (5 mm diameter) under a pressure of 2 Tonnes for 2 min. A Varian VK 7000 pharmaceutical dissolution instrument was used to monitor the release of APIs. The TCP monolith was placed in a stainless-steel basket, attached to the spindle, and immersed in 900 mL of buffer solution at 37 °C. Aliquots (1.5 mL) were taken at different time intervals. The media was not replaced. The aliquots were analyzed by UV-Vis spectroscopy; λ_{max} 276 nm for Diclofenac. The concentration of the API in each aliquot was determined using a calibration curve. The dissolution of the TCP was studied using 0.05 M phosphate buffer (pH 6.8), 0.01 M citrate buffer (pH 5.5), and 0.01 M citrate buffer with 0.05% of sodium dodecyl sulfate (pH 5.5).

Intrinsic dissolution rates were determined using a Woods apparatus (4.0 mm diameter) at 50 rpm using a Varian VK 7000 pharmaceutical dissolution instrument. Materials were pressed to 1.5 Tonnes for 1 min. 900 mL of buffer solution at 37 °C was used, and aliquots of 1.5 mL were taken at varying time intervals which were dependent on the material being analyzed. Concentrations were determined via UV-vis spectroscopy. Rates were determined from the slope of a linear concentration vs. time plot. Intrinsic dissolution of TCPs was studied using 0.05 M phosphate buffer (pH 6.8), and 0.05 M phosphate buffer with 0.05% EDTA (pH 6.8).

Cytotoxicity studies were performed with human non-fetal skin fibroblasts (NHF) (Coriell Institute for Medical Research, Cat. No. AG09309) which were grown at 5% CO_2 and 37 °C and cultured in Eagle's Minimum Essential Medium with Earle's salts and non-essential amino acids supplemented with 15% (v/v) fetal bovine serum (Thermo Scientific, Waltham, MA, USA) and 10 mg/mL gentamicin (Gibco BRL, VWR, Mississauga, ON, Canada). WST-1 assays were performed according to the manufacturer's protocol (Roche Applied Sciences, Indianapolis, IN, USA) to examine cell viability following TCP treatment. Briefly, NHF cells seeded on 96-well cell culture plates were treated for 48 h and incubated with WST-1 reagent for 3 h in the absence of light. The proportion of metabolically active cells was observed by detecting formazan through absorbance readings at 450 nm on a Wallac Victor3 1420 Multilabel Counter (PerkinElmer, Waltham, MA, USA). Microscopic imaging was conducted with a Leica DMI6000 B inverted microscope (Leica Microsystems, Concord, ON, Canada), following the addition of 10 µM Hoechst nuclear stain. Statistical analysis was conducted with GraphPad Prism 6 statistical software, where values of $P < 0.05$ were taken as significant. A 2-way analysis of variance with Dunnett's test was utilized and sample means were compared to DMSO controls.

Scanning electron microscopy (SEM) images were collected using a Quanta 200 FEG instrument from FEI Company under low-vacuum conditions. Note: pores/holes observed in the images are from the background tape used to mount the samples and are not reflective of the sample.

1. Crystallographic Data

1.1 Crystal Structures

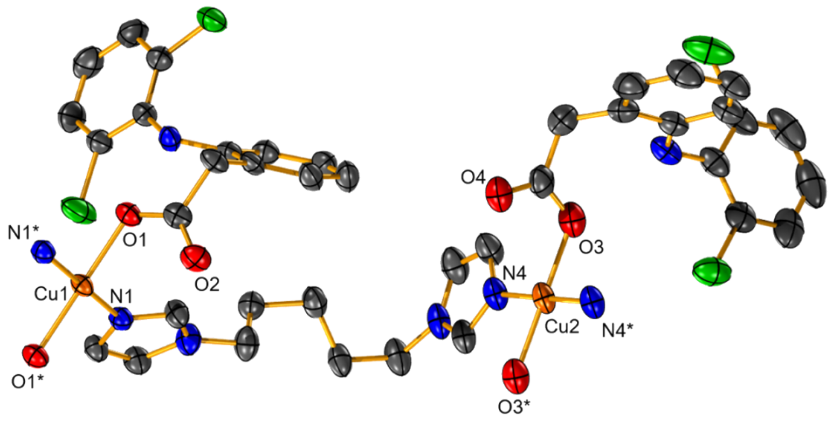

Figure S1: Coordination environments of the Cu(II) ions in $Cu(Diclo)_2(biim\text{-}5)$. Ellipsoids shown at 50% probability and H atoms omitted for clarity..

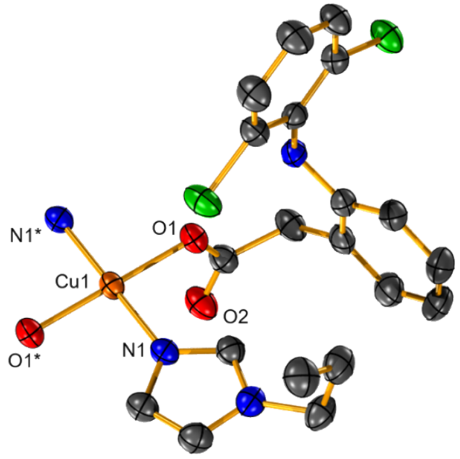

Figure S2: Coordination environment of the Cu(II) ion in $Cu(Diclo)_2(biim\text{-}6)\cdot(MeOH)_2$. Ellipsoids shown at 50% probability and H atoms and solvent omitted for clarity.

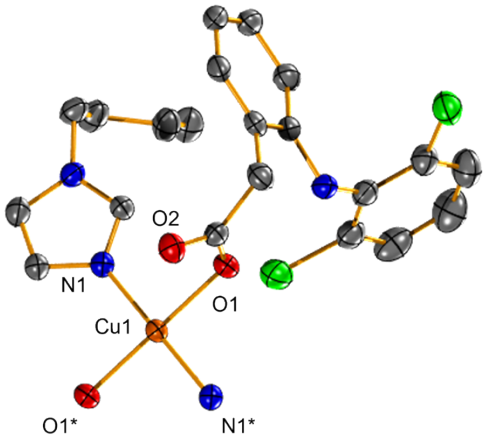

Figure S3: Coordination environment of the Cu(II) ion in $Cu(Diclo)_2(biim\text{-}8)\cdot(MeOH)_2$. Ellipsoids shown at 50% probability. H atoms and solvent omitted for clarity.

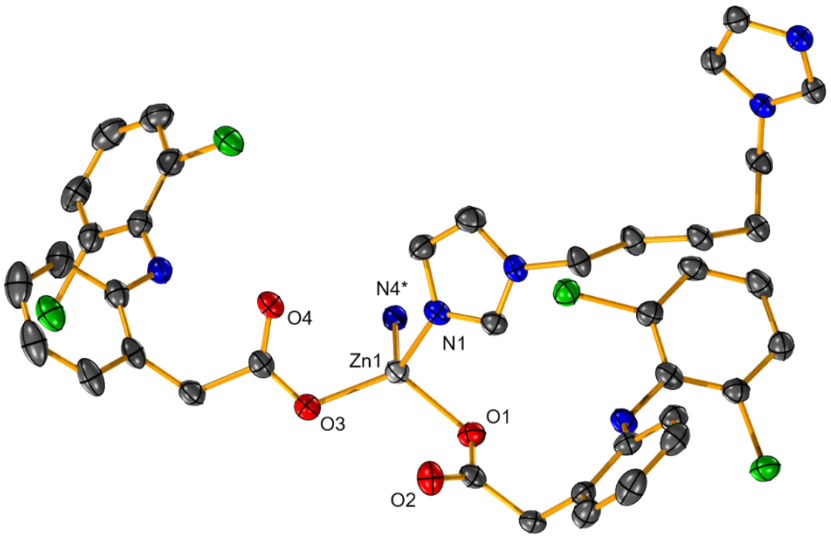

Figure S4: Coordination environment of the Zn(II) ion in $Zn(Diclo)_2(biim\text{-}5)$. Ellipsoids shown at 50% probability and H atoms omitted for clarity.

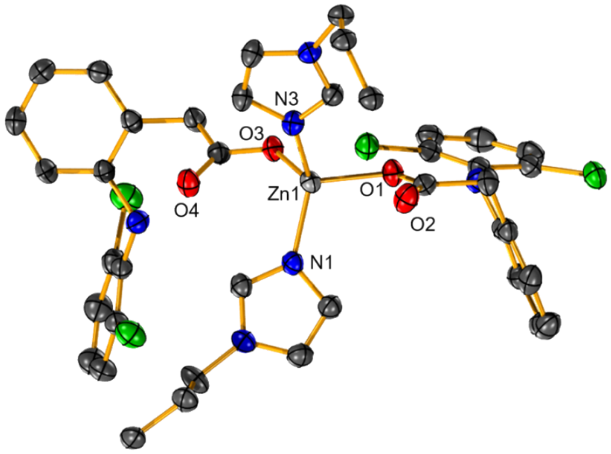

Figure S5: Coordination environment of the Zn(II) ion in $Zn(Diclo)_2(biim\text{-}6)\cdot(MeOH)$. Ellipsoids shown at 50% probability. H atoms and solvent omitted for clarity.

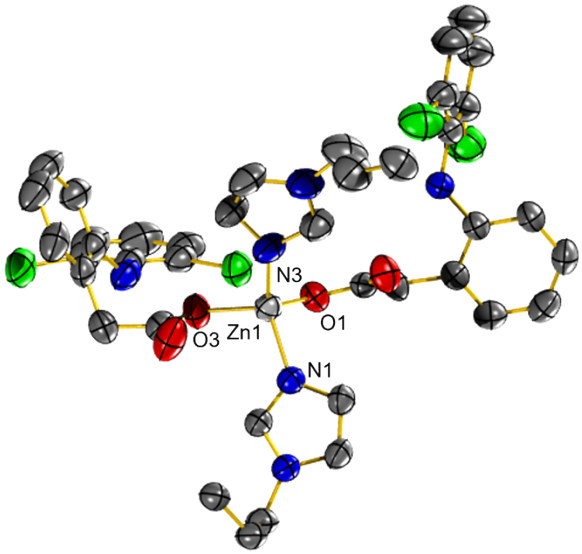

Figure S6: Coordination environment of the Zn(II) ion in $Zn(Diclo)_2$(biim-6)·(EtOH). Ellipsoids shown at 50% probability. H atoms and solvent omitted for clarity.

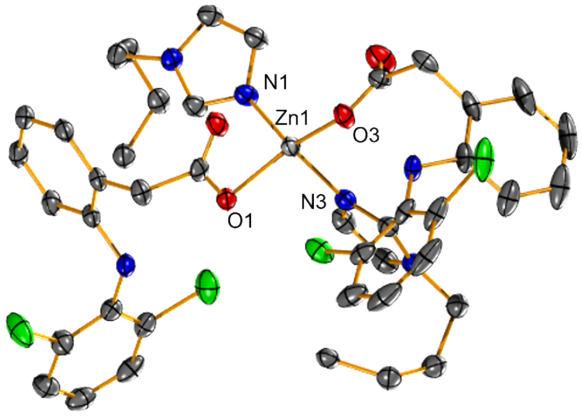

Figure S7: Coordination environment of the Zn(II) ion in $Zn(Diclo)_2$(biim-8). Ellipsoids shown at 50% probability and H atoms omitted for clarity.

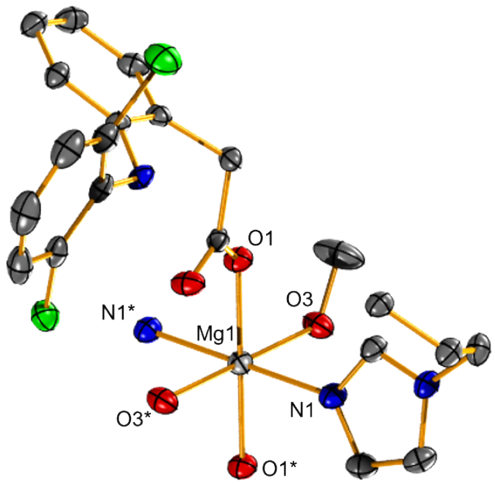

Figure S8: Coordination environment of the Mg(II) ion in $Mg(Diclo)_2(biim\text{-}6)_2(MeOH)_2$. Ellipsoids shown at 50% probability and H atoms omitted for clarity.

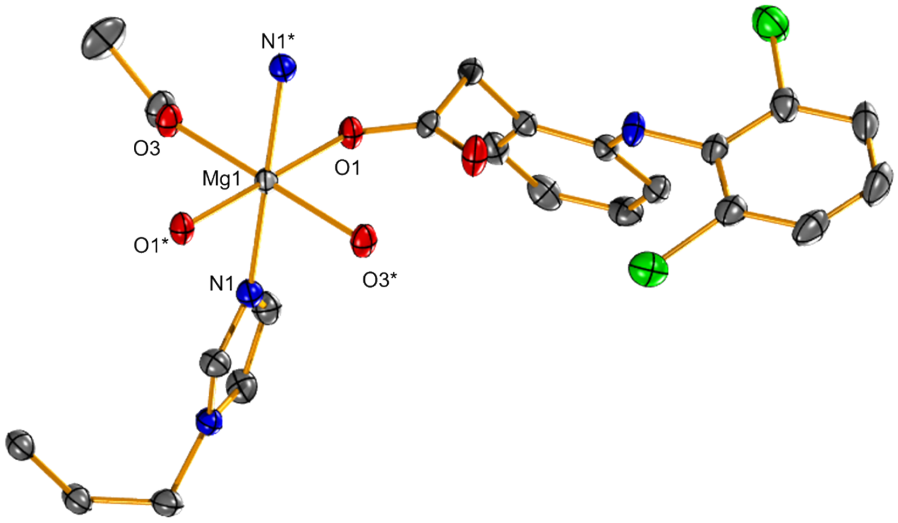

Figure S9: Coordination environment of the Mg(II) ion in $Mg(Diclo)_2(biim\text{-}6)_2(EtOH)_2$. Ellipsoids shown at 50% probability and H atoms omitted for clarity.

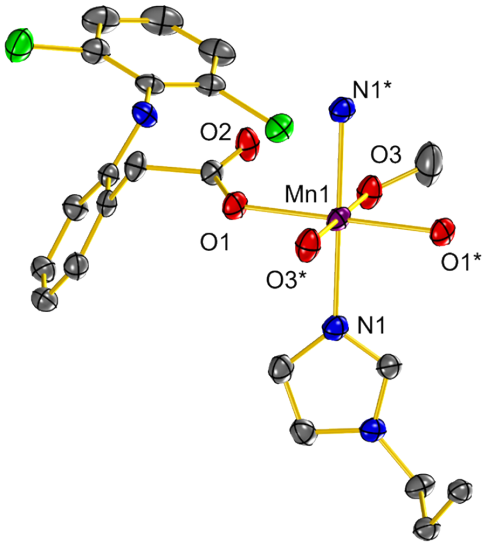

Figure S10: Coordination environment of the Mn(II) ion in $Mn(Diclo)_2(biim\text{-}6)_2(MeOH)_2$. Ellipsoids shown at 50% probability and H atoms omitted for clarity.

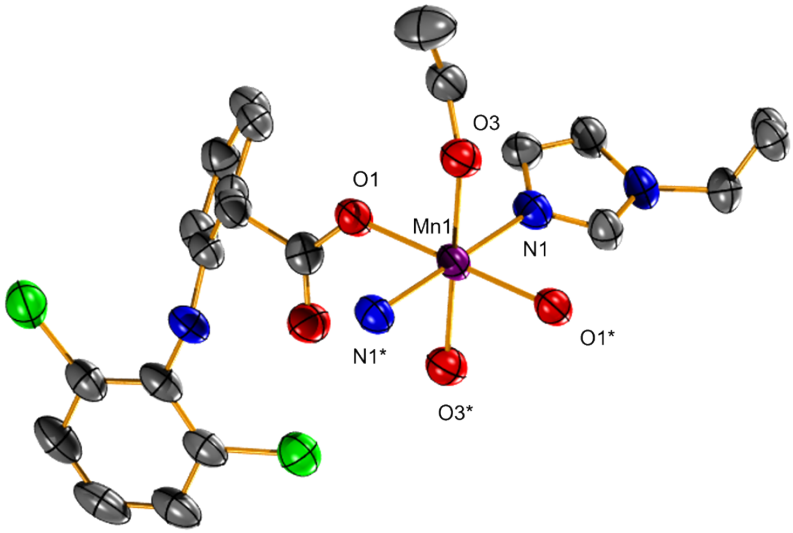

Figure S11: Coordination environment of the Mn(II) ion in $Mn(Diclo)_2(biim\text{-}6)_2(EtOH)_2$. Ellipsoids shown at 50% probability and H atoms omitted for clarity.

1.2 Table of Parameters

	CuDiclo5	CuDiclo6·MeOH	CuDiclo8·MeOH	ZnDiclo5	ZnDiclo6·MeOH
CCDC deposition number	2237930	2237929	2237924	2237931	2237932
Empirical formula	$C_{39}H_{36}Cl_4CuN_6O_4$	$C_{42}H_{46}Cl_4CuN_6O_6$	$C_{44}H_{50}Cl_4CuN_6O_6$	$C_{39}H_{36}Cl_4N_6O_4Zn$	$C_{41}H_{42}Cl_4N_6O_5Zn$
Formula weight	858.08	936.19	964.24	859.91	905.97
Crystal system	monoclinic	monoclinic	triclinic	monoclinic	monoclinic
Space group	$P2_1/c$	$P2_1/n$	P-1	$P2_1/n$	$P2_1/n$
a/Å	21.7971(5)	8.1316(3)	8.1744(3)	15.7556(3)	14.7461(3)
b/Å	8.3133(2)	10.8394(3)	11.9929(5)	15.5699(3)	14.5959(3)
c/Å	21.5270(6)	24.3849(7)	13.8763(6)	16.1773(3)	19.2358(3)
α/°	90	90	68.678(2)	90	90
β/°	90.584(2)	97.503(3)	77.480(2)	109.828(2)	97.599(2)
γ/°	90	90	81.887(2)	90	90
Volume/Å^3	3900.62(17)	2130.92(12)	1234.20(9)	3733.23(13)	4103.81(14)
Z	4	2	1	4	4
ρ_{calc}g/cm^3	1.461	1.459	1.297	1.530	1.466
μ/mm^{-1}	3.714	3.482	3.021	3.968	3.657
F(000)	1764.0	970.0	501.0	1768.0	1872.0
Crystal size/mm^3	0.3 × 0.2 × 0.1	0.3 × 0.2 × 0.05	0.5 × 0.2 × 0.03	0.2 × 0.2 × 0.1	0.4 × 0.4 × 0.2
2Θ range for data collection/°	8.112 to 133.192	7.314 to 133.19	6.95 to 149.562	6.768 to 136.498	7.118 to 148.996
Index ranges	-25 ≤ h ≤ 25, -9 ≤ k ≤ 9, -24 ≤ l ≤ 25	-9 ≤ h ≤ 8, -12 ≤ k ≤ 12, -29 ≤ l ≤ 29	-10 ≤ h ≤ 10, -14 ≤ k ≤ 14, -17 ≤ l ≤ 17	-18 ≤ h ≤ 18, -18 ≤ k ≤ 18, -19 ≤ l ≤ 19	-17 ≤ h ≤ 18, -18 ≤ k ≤ 18, -24 ≤ l ≤ 24
Reflections collected	183242	79116	22244	222774	226781
Independent reflections	6885 [R_{int} = 0.1367, R_{sigma} = 0.0338]	3763 [R_{int} = 0.1038, R_{sigma} = 0.0290]	4990 [R_{int} = 0.0650, R_{sigma} = 0.0475]	6828 [R_{int} = 0.1289, R_{sigma} = 0.0268]	8387 [R_{int} = 0.1159, R_{sigma} = 0.0259]
Data/restraints/parameters	6885/1/489	3763/1/277	4990/0/279	6828/0/496	8387/0/524
Goodness-of-fit on F^2	1.079	1.072	1.064	1.059	1.027
Final R indexes [I>=2σ (I)]	R_1 = 0.0608, wR_2 = 0.1627	R_1 = 0.0526, wR_2 = 0.1443	R_1 = 0.0585, wR_2 = 0.1520	R_1 = 0.0542, wR_2 = 0.1465	R_1 = 0.0524, wR_2 = 0.1407
Final R indexes [all data]	R_1 = 0.0717, wR_2 = 0.1752	R_1 = 0.0595, wR_2 = 0.1532	R_1 = 0.0692, wR_2 = 0.1613	R_1 = 0.0580, wR_2 = 0.1519	R_1 = 0.0561, wR_2 = 0.1450
Largest diff. peak/hole / e Å^{-3}	0.96/-0.66	0.39/-0.57	0.67/-0.53	0.80/-0.58	0.45/-0.83

	ZnDiclo6·EtOH	ZnDiclo8	MnDiclo6·MeOH	MnDiclo6·EtOH	MgDiclo6·MeOH	MgDiclo6·EtOH
CCDC deposition number	2237933	2237926	2237934	2237927	2237925	2237928
Empirical formula	$C_{42}H_{44}Cl_4N_6O_5Zn$	$C_{42}H_{42}Cl_4N_6O_4Zn$	$C_{42}H_{46}Cl_4MnN_6O_6$	$C_{44}H_{50}Cl_4MnN_6O_6$	$C_{42}H_{46}Cl_4MgN_6O_6$	$C_{44}H_{50}Cl_4MgN_6O_6$
Formula weight	920.00	901.98	927.59	955.64	896.96	925.01
Crystal system	monoclinic	triclinic	monoclinic	monoclinic	monoclinic	monoclinic
Space group	$P2_1/n$	P-1	$P2_1/n$	$P2_1/n$	$P2_1/n$	$P2_1/n$
a/Å	14.82310(10)	11.3205(4)	8.5133(2)	8.5583(9)	8.48440(10)	8.50360(10)
b/Å	14.77870(10)	13.1000(5)	20.8959(7)	21.737(3)	20.9466(2)	21.7792(3)
c/Å	19.9676(2)	15.6723(6)	12.8879(4)	12.8769(19)	12.84190(10)	12.8123(2)
α/°	90	113.7270(10)	90	90	90	90
β/°	96.8790(10)	98.6240(10)	107.4090(10)	108.475(14)	107.4270(10)	108.489(2)
γ/°	90	97.2980(10)	90	90	90	90
Volume/Å^3	4342.74(6)	2058.10(13)	2187.65(11)	2272.1(5)	2177.50(4)	2250.38(6)
Z	4	2	2	2	2	2
ρ_{calc}g/cm^3	1.407	1.455	1.408	1.397	1.368	1.365
μ/mm^{-1}	3.464	3.625	0.599	4.965	3.053	2.970
F(000)	1904.0	932.0	962.0	994.0	936.0	968.0
Crystal size/mm^3	0.3 × 0.15 × 0.15	0.2 × 0.2 × 0.1	0.3 × 0.3 × 0.1	0.2 × 0.05 × 0.05	0.4 × 0.3 × 0.2	0.2 × 0.2 × 0.1
2Θ range for data collection/°	7.038 to 148.994	6.316 to 144.194	6.354 to 56.712	8.134 to 133.176	8.36 to 158.52	8.12 to 136.464
Index ranges	-17 ≤ h ≤ 18, -18 ≤ k ≤ 18, -24 ≤ l ≤ 24	-13 ≤ h ≤ 13, -16 ≤ k ≤ 16, -19 ≤ l ≤ 19	-11 ≤ h ≤ 11, -27 ≤ k ≤ 27, -17 ≤ l ≤ 17	-9 ≤ h ≤ 10, -25 ≤ k ≤ 25, -15 ≤ l ≤ 14	-10 ≤ h ≤ 9, -26 ≤ k ≤ 26, -16 ≤ l ≤ 16	-9 ≤ h ≤ 10, -26 ≤ k ≤ 26, -15 ≤ l ≤ 15
Reflections collected	93894	46068	137306	24612	40598	45917
Independent reflections	8888 [R_{int} = 0.0652, R_{sigma} = 0.0252]	8063 [R_{int} = 0.0361, R_{sigma} = 0.0222]	5427 [R_{int} = 0.0417, R_{sigma} = 0.0120]	4000 [R_{int} = 0.1870, R_{sigma} = 0.1128]	4696 [R_{int} = 0.0473, R_{sigma} = 0.0241]	4132 [R_{int} = 0.0675, R_{sigma} = 0.0293]
Data/restraints/parameters	8888/113/573	8063/48/522	5427/3/276	4000/3/285	4696/3/272	4132/9/285
Goodness-of-fit on F^2	1.043	1.051	1.075	0.967	1.072	1.048
Final R indexes [I>=2σ (I)]	R_1 = 0.0486, wR_2 = 0.1357	R_1 = 0.0361, wR_2 = 0.0943	R_1 = 0.0311, wR_2 = 0.0802	R_1 = 0.0754, wR_2 = 0.1829	R_1 = 0.0431, wR_2 = 0.1135	R_1 = 0.0346, wR_2 = 0.0893
Final R indexes [all data]	R_1 = 0.0566, wR_2 = 0.1454	R_1 = 0.0391, wR_2 = 0.0968	R_1 = 0.0369, wR_2 = 0.0852	R_1 = 0.1362, wR_2 = 0.2346	R_1 = 0.0463, wR_2 = 0.1169	R_1 = 0.0421, wR_2 = 0.0942
Largest diff. peak/hole / e Å^{-3}	0.33/-0.45	0.75/-0.74	0.39/-0.33	0.81/-0.69	0.35/-0.59	0.22/-0.29

1.3 Packing Diagrams

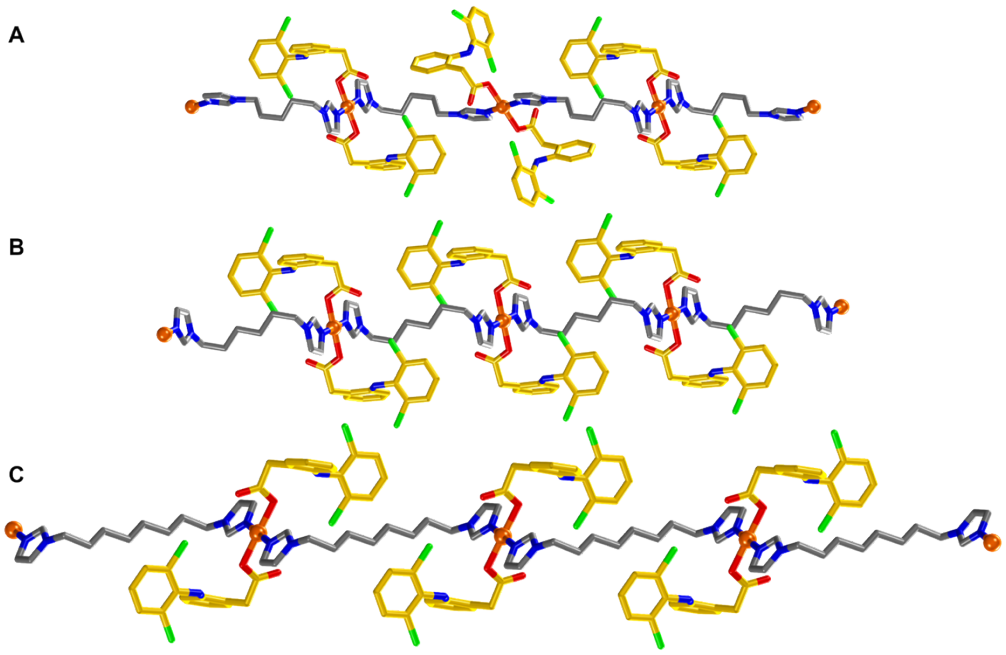

Figure S12. Single crystal structures of TCPs, a) $Cu(Diclo)_2(biim\text{-}5)$, b) $Cu(Diclo)_2(biim\text{-}6)\cdot(MeOH)_2$, $Cu(Diclo)_2(biim\text{-}8)\cdot(MeOH)_2$. Cu = orange, N = blue, O = red, Cl = green, bis-imidazole and Diclofenac C-atoms are shown in silver and gold, respectively. H atoms and solvent omitted for clarity.

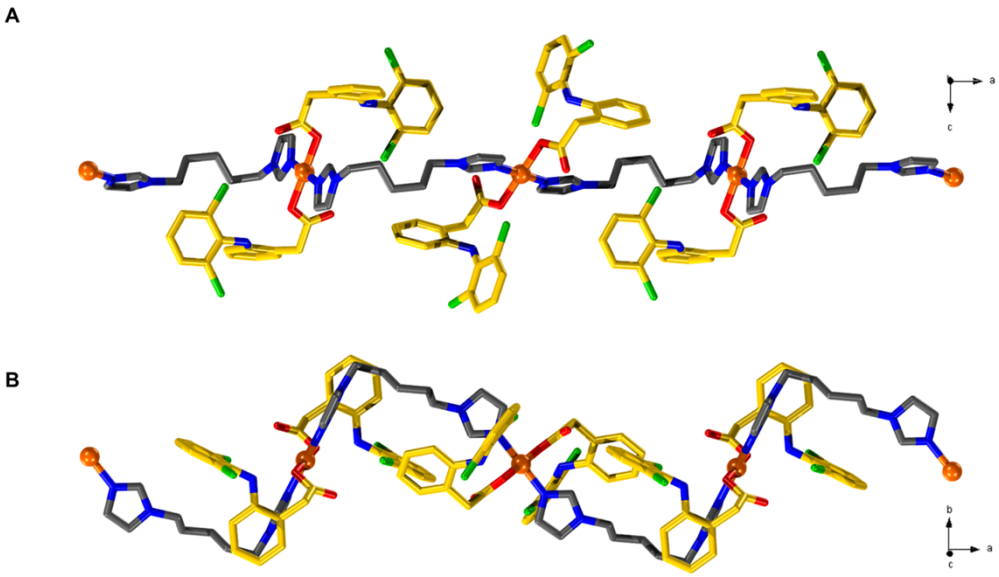

Figure S13. One-dimensional chain of $Cu(Diclo)_2(biim\text{-}5)$ as viewed a) along the b-axis, and b) along the c-axis. Cu = orange, N = blue, O = red, Cl = green, bis-imidazole and Diclofenac C-atoms are shown in silver and gold, respectively. H atoms omitted for clarity.

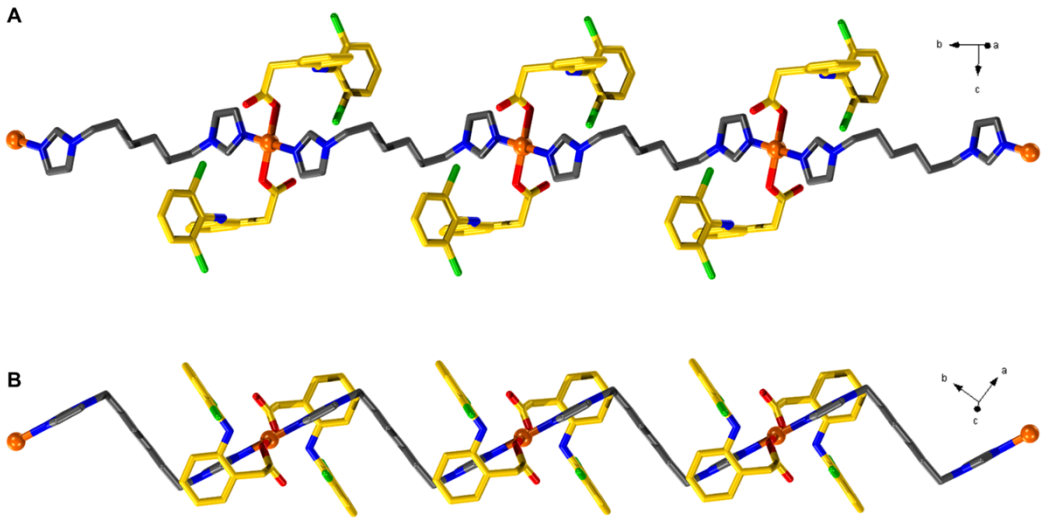

Figure S14. One-dimensional chain of $Cu(Diclo)_2(biim\text{-}6)\cdot(MeOH)_2$ as viewed a) along the a-axis, and b) along the c-axis. Cu = orange, N = blue, O = red, Cl = green, bis-imidazole and Diclofenac C-atoms are shown in silver and gold, respectively. H atoms and solvent omitted for clarity.

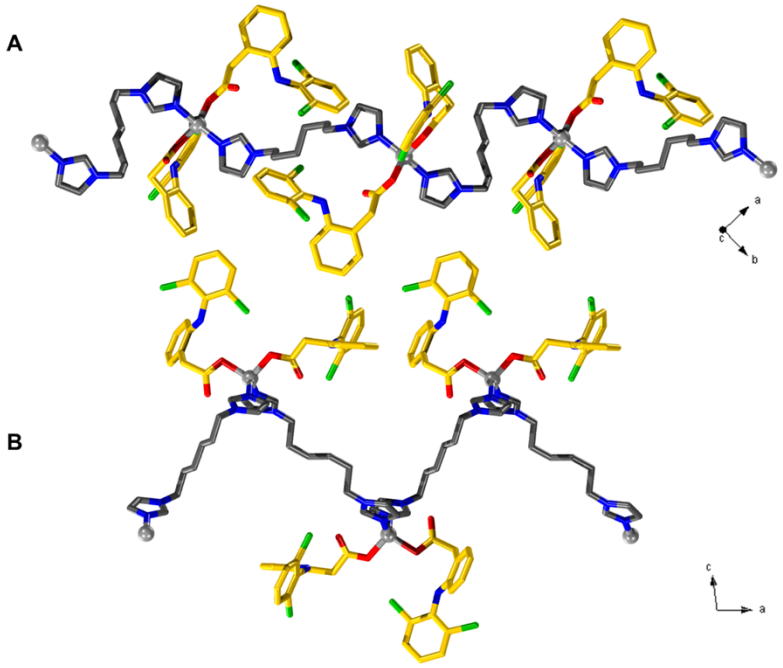

Figure S15. One-dimensional chain of $Zn(Diclo)_2(biim\text{-}6)\cdot(MeOH)$ as viewed a) along the c-axis, and b) along the b-axis. Zn = grey, N = blue, O = red, Cl = green, bis-imidazole and Diclofenac C-atoms are shown in silver and gold, respectively. H atoms and solvent omitted for clarity.

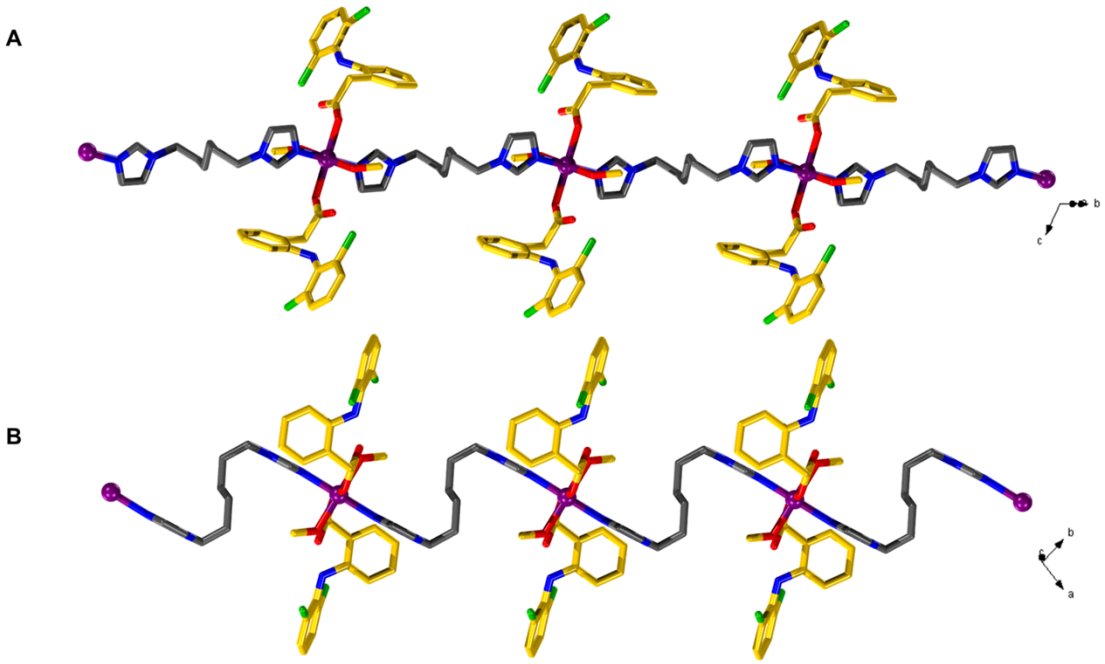

Figure S16. One-dimensional chain of $Mn(Diclo)_2(biim\text{-}6)(MeOH)_2$ as viewed a) along the a-axis, and b) along the c-axis. Mn = purple, N = blue, O = red, Cl = green, bis-imidazole and Diclofenac C-atoms are shown in silver and gold, respectively. H atoms omitted for clarity.

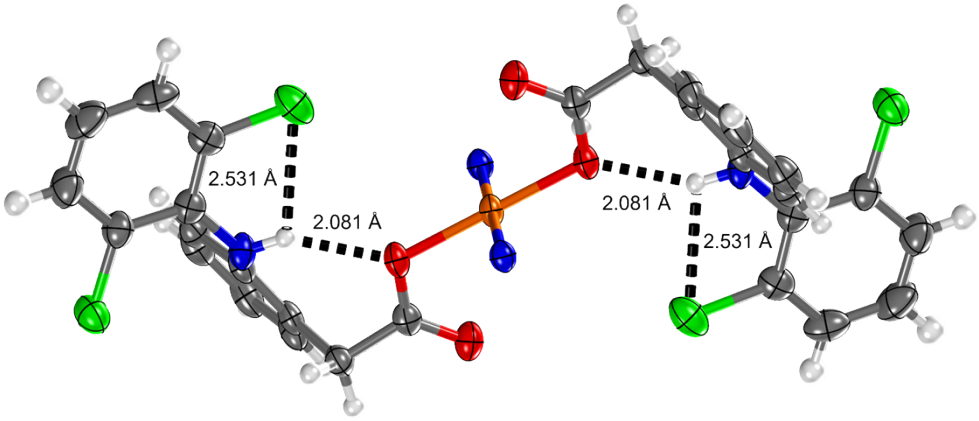

Figure S17. Coordination environment in $Cu(Diclo)_2(biim\text{-}8)\cdot(MeOH)_2$ showing intramolecular H-bonding interactions of Diclofenac.

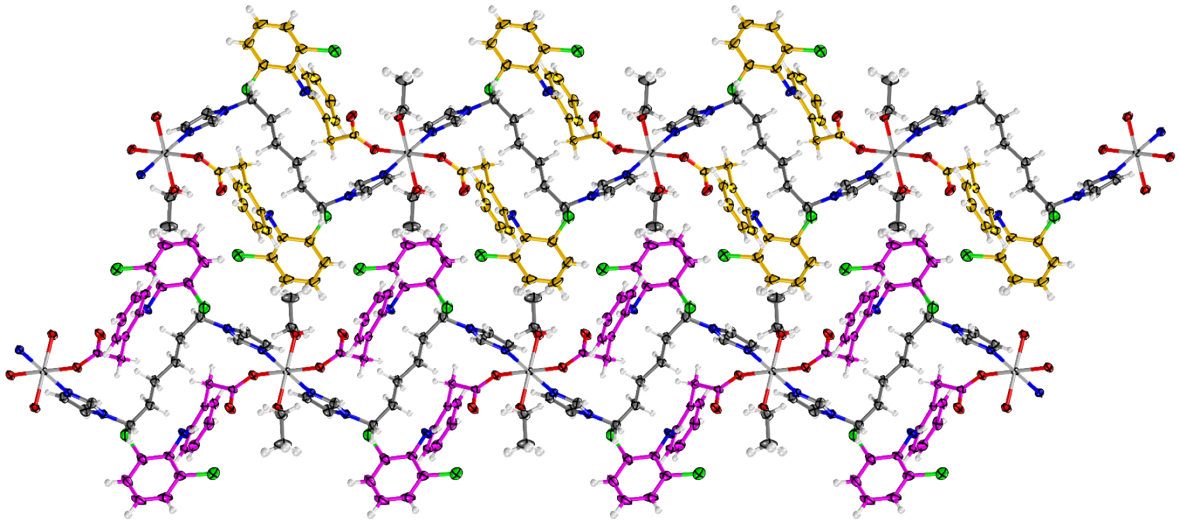

Figure S18. Packing of parallel polymeric chains in $Mg(Diclo)_2(biim\text{-}6)(EtOH)_2$ as seen along the a-axis. Diclofenac C atoms colored pink in one strand and yellow in the other to depict close packing of the chains. Mg = light grey, N = blue, O = red, Cl = green, C (bis-imidazole linker) = grey.

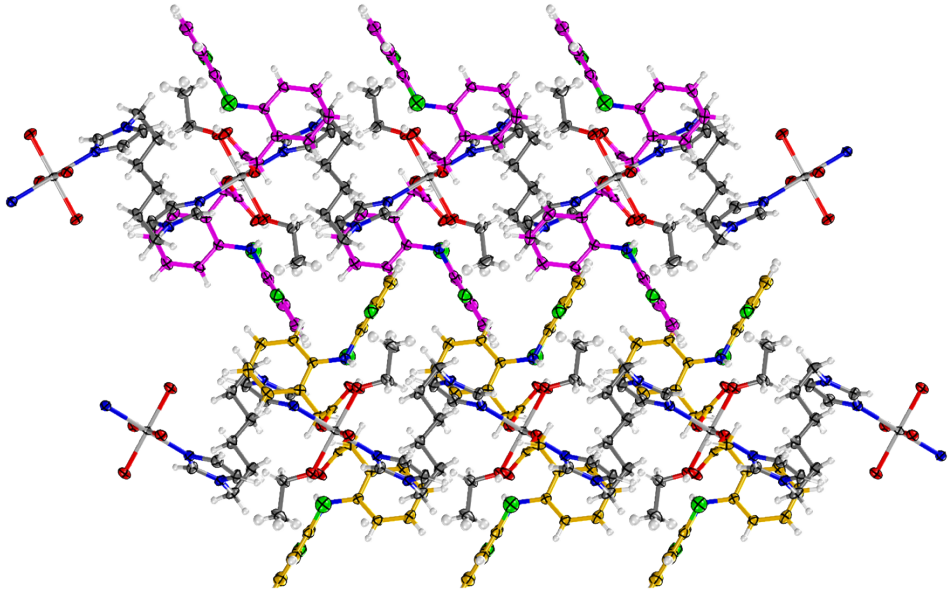

Figure S19. Packing of parallel polymeric chains in $Mg(Diclo)_2(biim\text{-}6)(EtOH)_2$ as seen along the c-axis. Diclofenac C atoms colored pink in one strand and yellow in the other to depict close packing of the chains. Mg = light grey, N = blue, O = red, Cl = green, C (bis-imidazole linker) = grey.

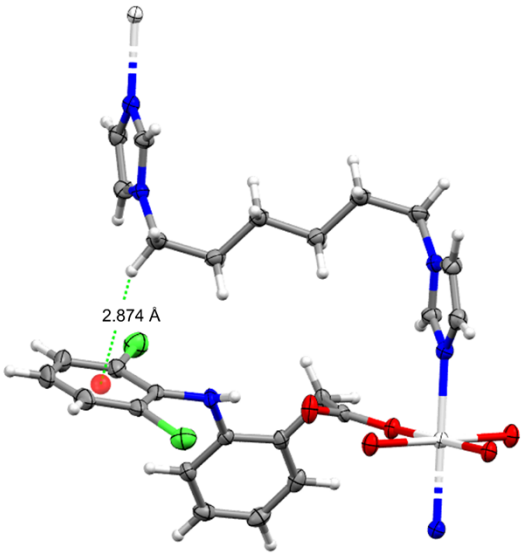

Figure S20. C-H···π interaction between Diclofenac centroid (C9-C14) and H atom of bis-imidazole linker in $Mg(Diclo)_2(biim\text{-}6)(EtOH)_2$. Mg = light grey, N = blue, O = red, Cl = green, C = grey.

2. Infrared Spectroscopy

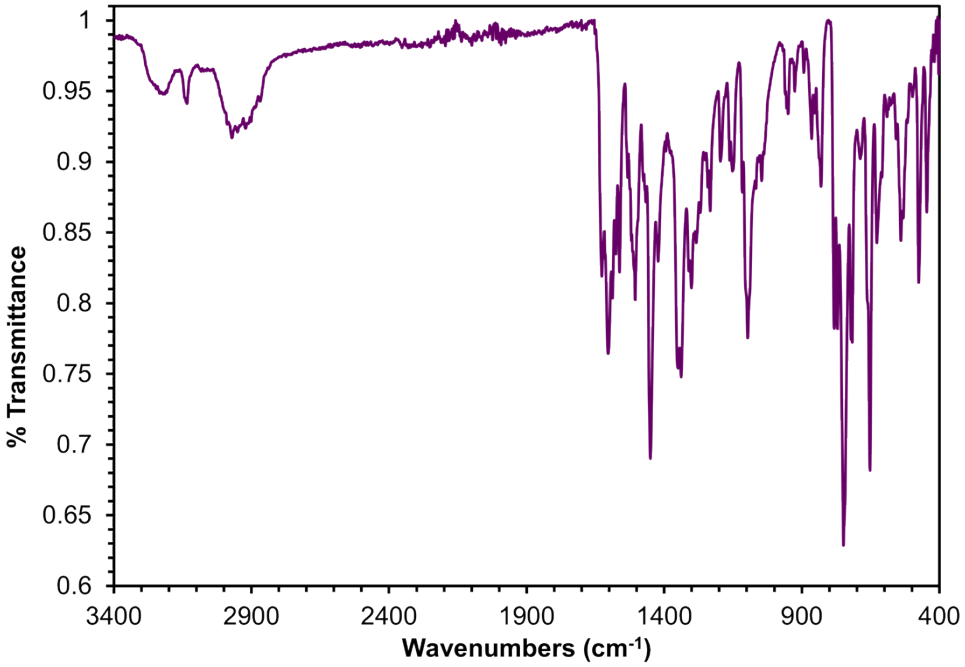

Figure S21: Infrared spectrum of $Cu(Diclo)_2(biim\text{-}5)$.

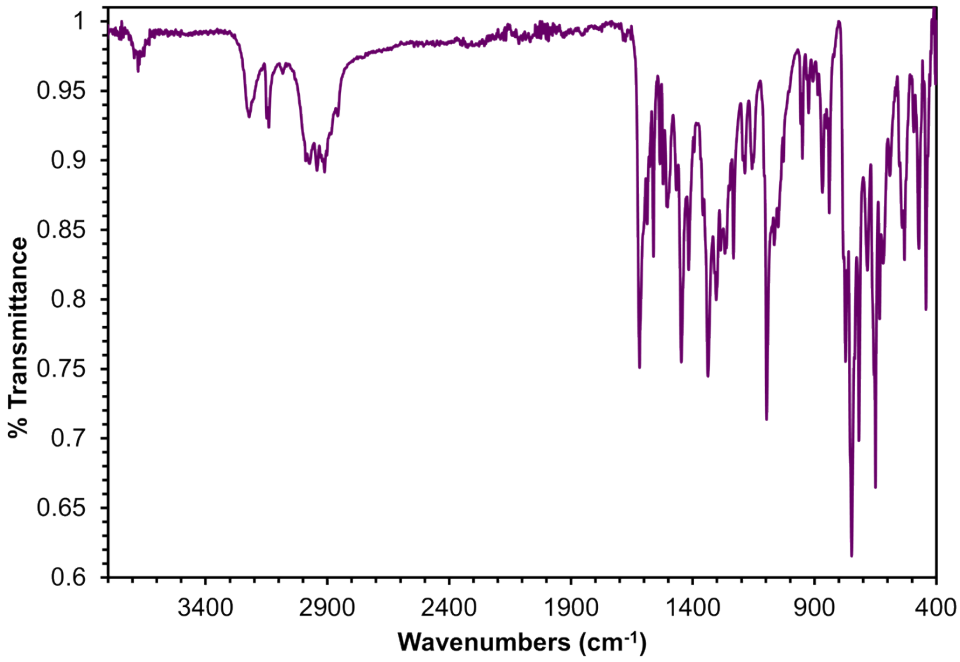

Figure S22: Infrared spectrum of $Cu(Diclo)_2(biim\text{-}6)\cdot(MeOH)_2$.

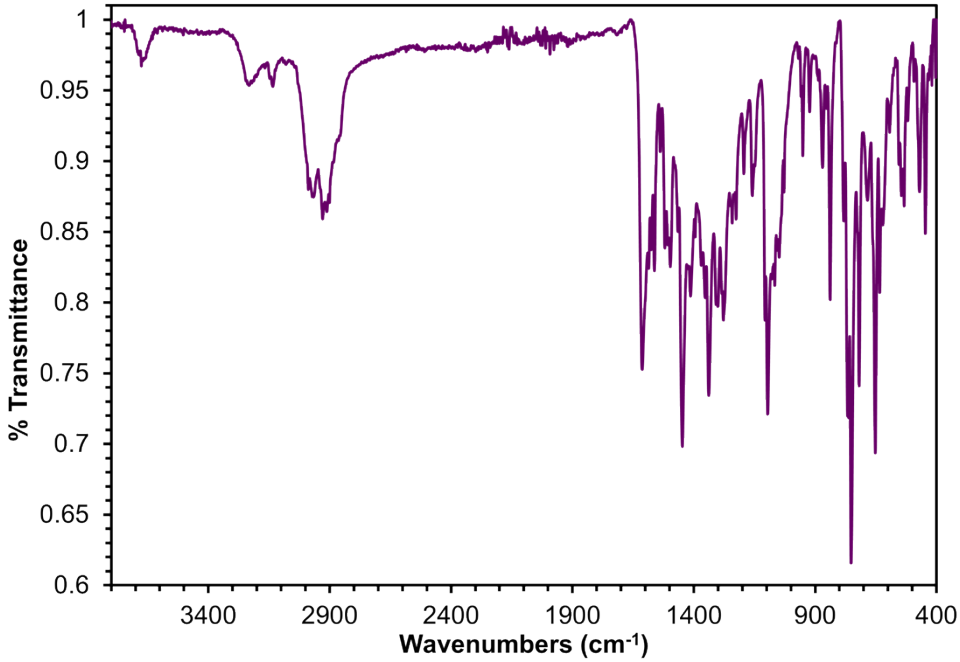

Figure S23: Infrared spectrum of $Cu(Diclo)_2(biim\text{-}8)\cdot(MeOH)_2$.

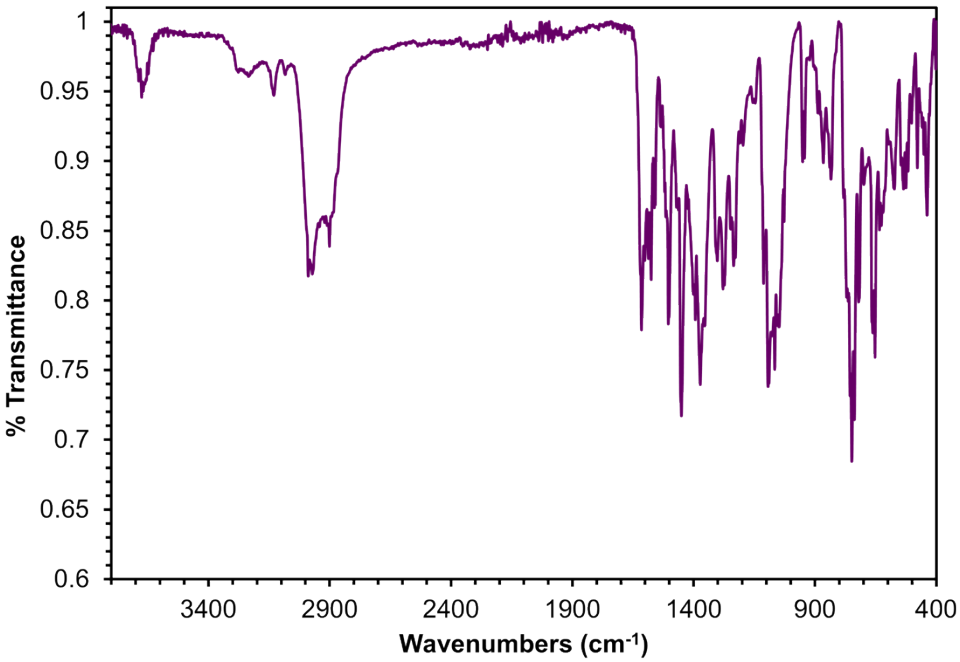

Figure S24: Infrared spectrum of $Zn(Diclo)_2(biim\text{-}5)$.

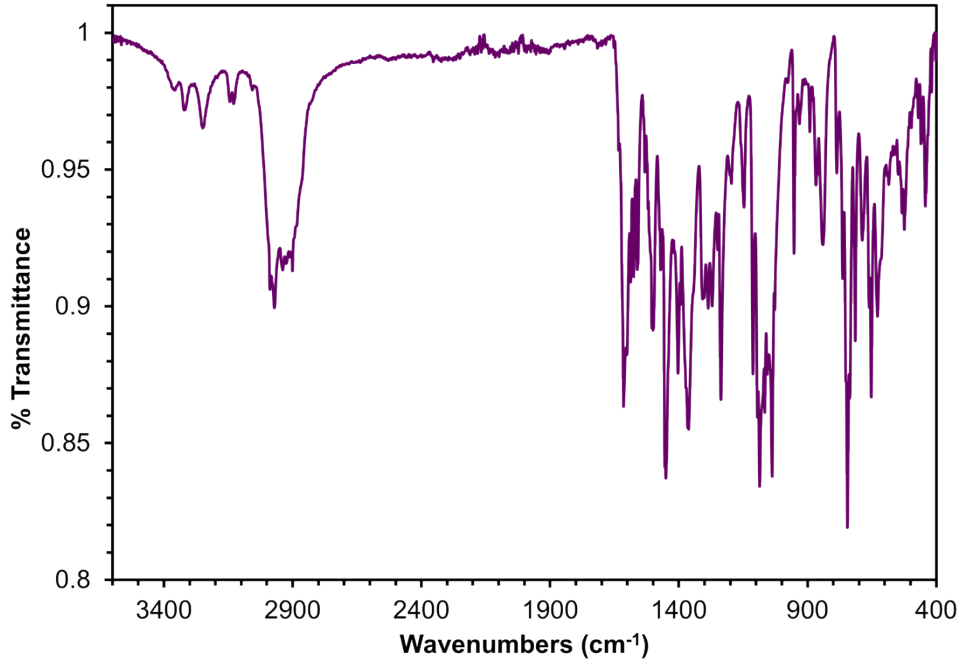

Figure S25: Infrared spectrum of $Zn(Diclo)_2(biim\text{-}6)\cdot(MeOH)$.

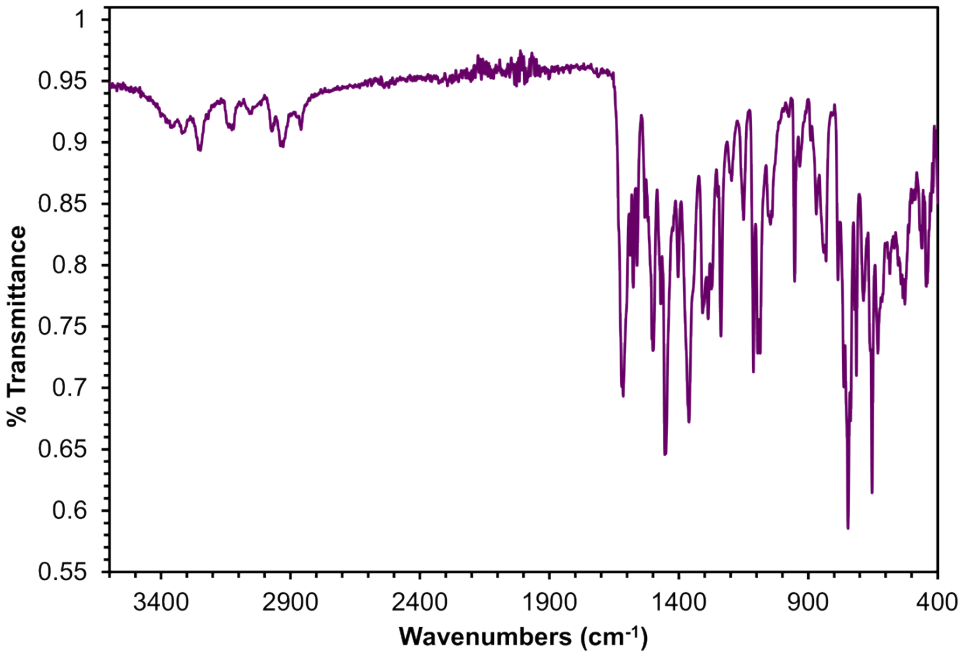

Figure S26: Infrared spectrum of $Zn(Diclo)_2(biim\text{-}6)\cdot(EtOH)$.

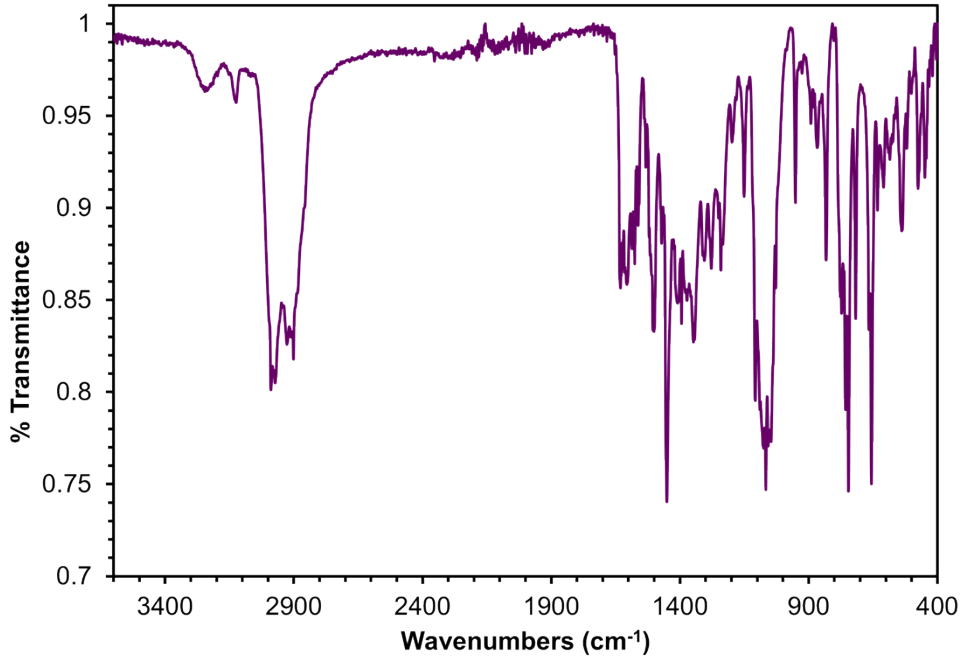

Figure S27: Infrared spectrum of $Zn(Diclo)_2(biim\text{-}8)$.

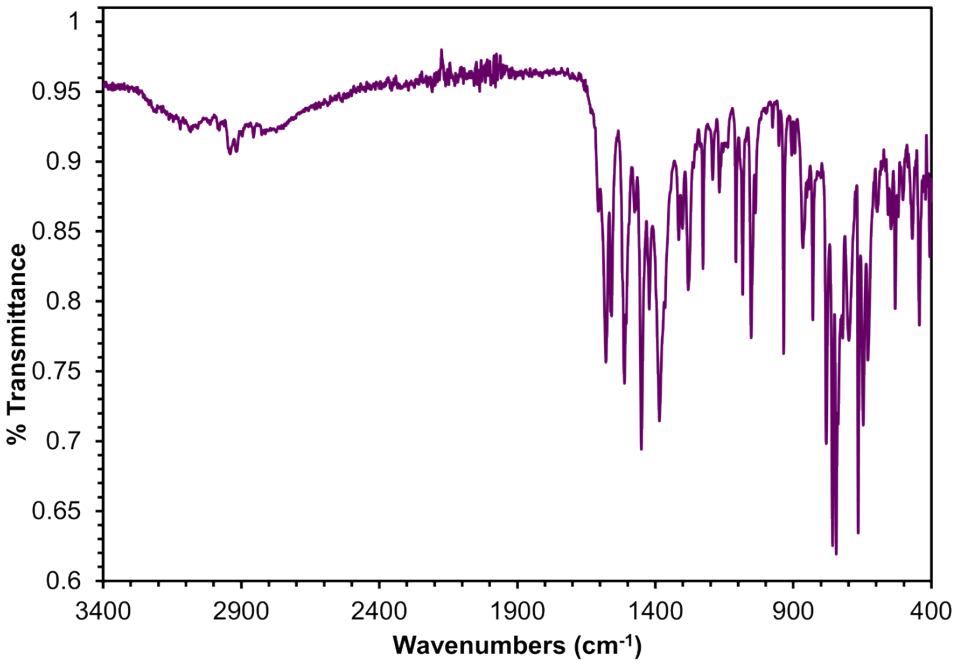

Figure S28: Infrared spectrum of $Mg(Diclo)_2(biim\text{-}6)(MeOH)_2$.

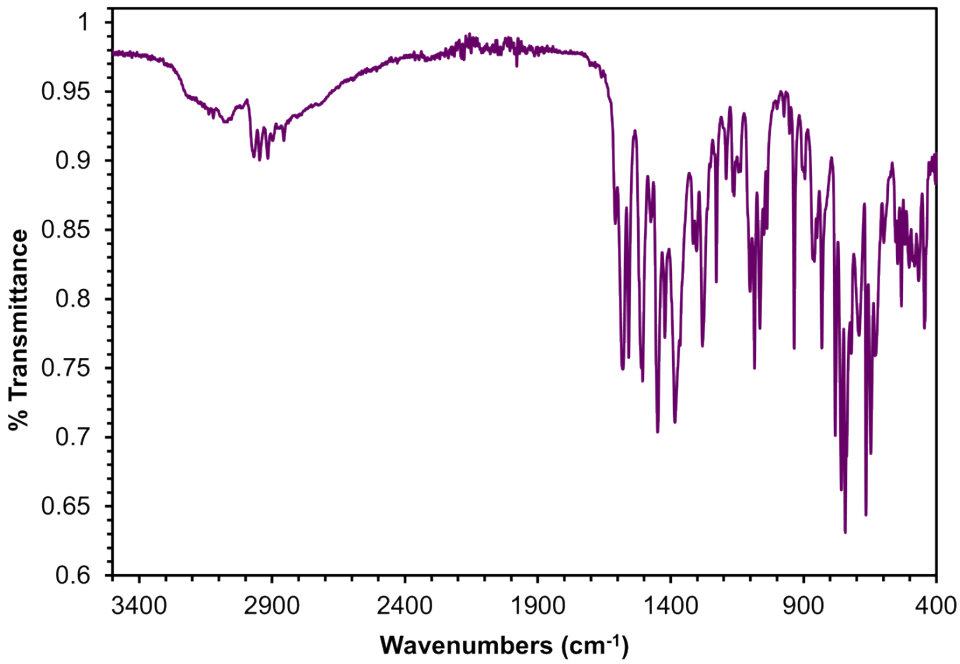

Figure S29: Infrared spectrum of $Mg(Diclo)_2(biim\text{-}6)(EtOH)_2$.

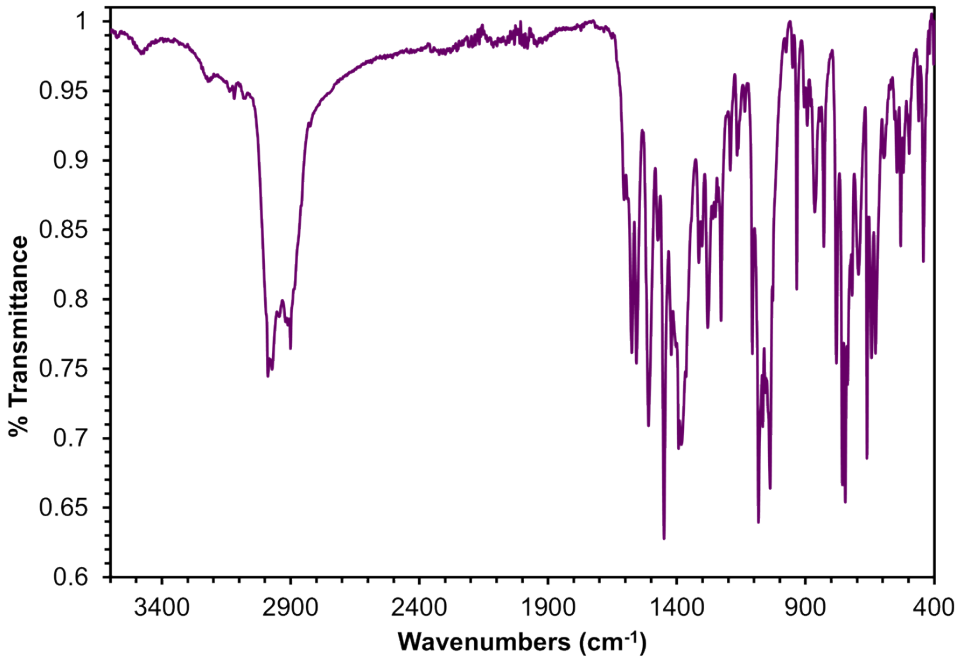

Figure S30: Infrared spectrum of $Mn(Diclo)_2(biim\text{-}6)(MeOH)_2$.

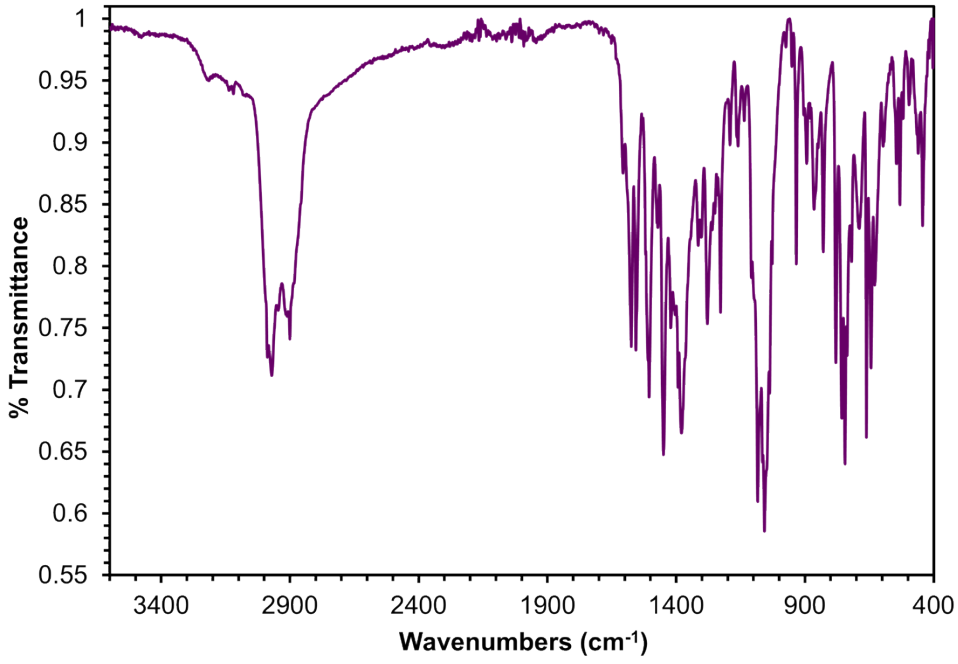

Figure S31: Infrared spectrum of $Mn(Diclo)_2(biim\text{-}6)(EtOH)_2$.

3. Powder X-Ray Diffraction

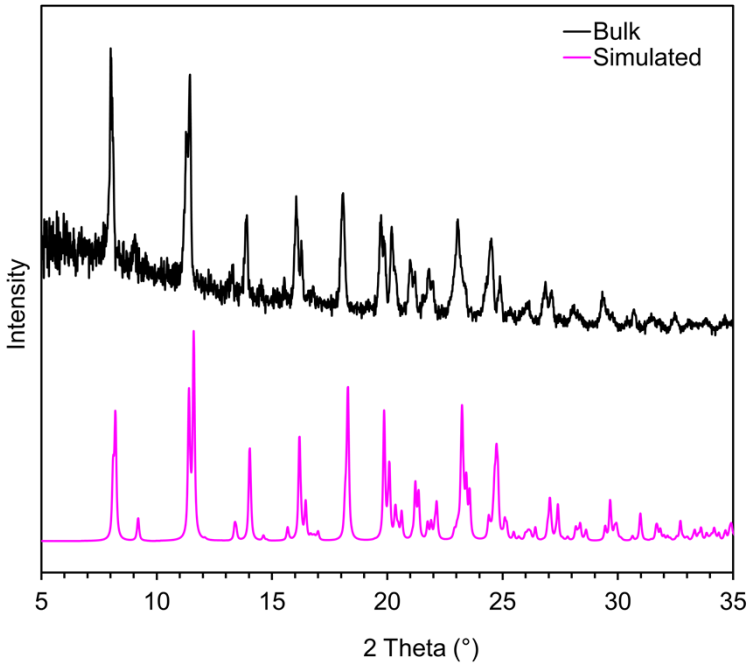

Figure S32: Comparison of Powder XRD pattern (CuKα radiation, λ = 1.5418 Å) from single crystal (simulated) and the bulk powder sample of $Cu(Diclo)_2(biim\text{-}5)$.

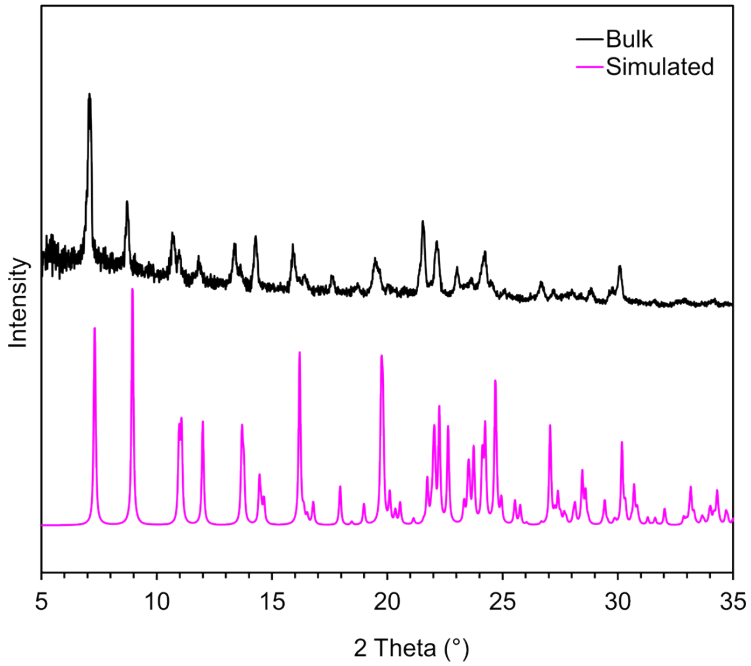

Figure S33: Comparison of Powder XRD pattern (CuKα radiation, λ = 1.5418 Å) from single crystal (simulated) and the bulk powder sample of $Cu(Diclo)_2(biim\text{-}6)\cdot(MeOH)_2$.

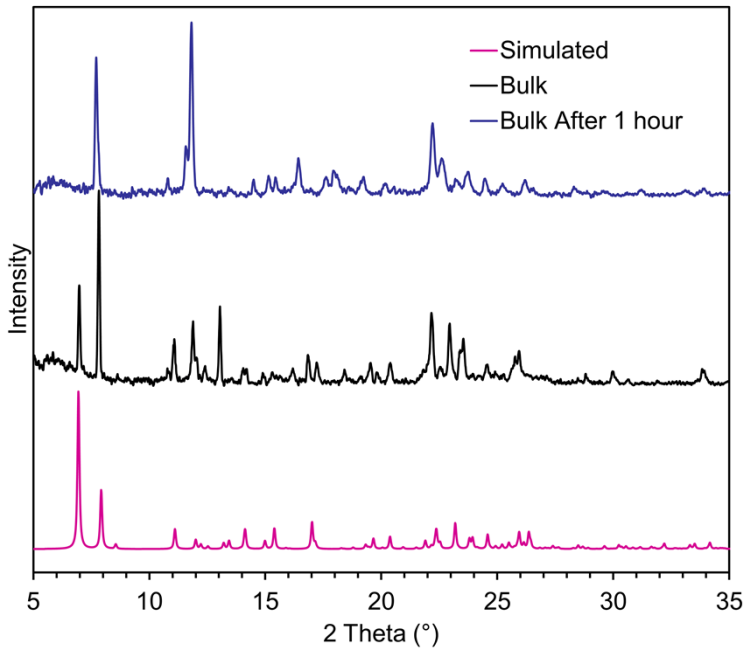

Figure S34. Comparison of Powder XRD pattern (CuKα radiation, λ = 1.5418 Å) from single crystal (simulated) and the bulk powder sample of $Cu(Diclo)_2(biim\text{-}8)\cdot(MeOH)_2$. After 1 hour, the bulk powder phase desolvated and a new phase formed.

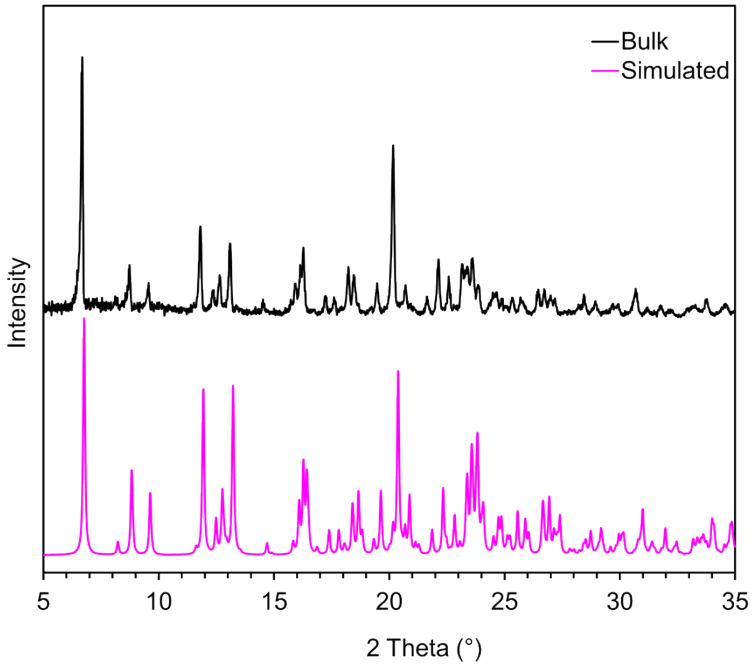

Figure S35: Comparison of Powder XRD pattern (CuKα radiation, λ = 1.5418 Å) from single crystal (simulated) and the bulk powder sample of $Zn(Diclo)_2(biim\text{-}5)$.

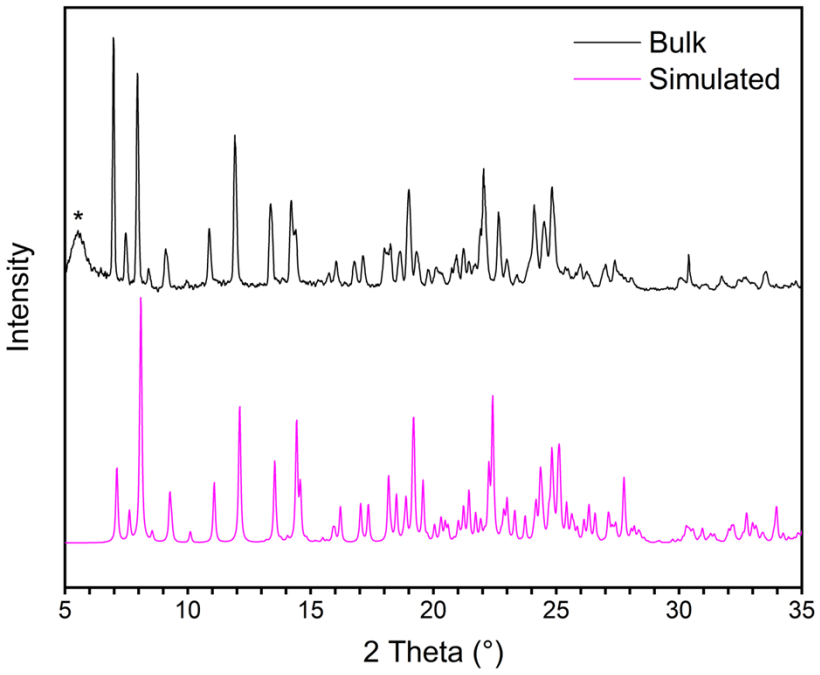

Figure S36: Comparison of Powder XRD pattern (CuKα radiation, λ = 1.5418 Å) from single crystal (simulated) and the bulk powder sample of $Zn(Diclo)_2(biim\text{-}6)\cdot(MeOH)$ (*Kapton film).

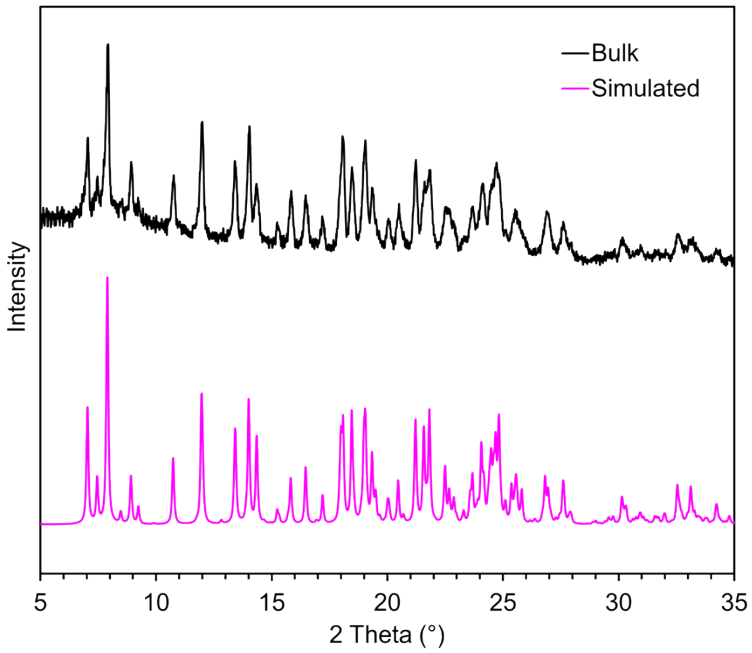

Figure S37: Comparison of Powder XRD pattern (CuKα radiation, λ = 1.5418 Å) from single crystal (simulated) and the bulk powder sample of $Zn(Diclo)_2(biim\text{-}6)\cdot(EtOH)$.

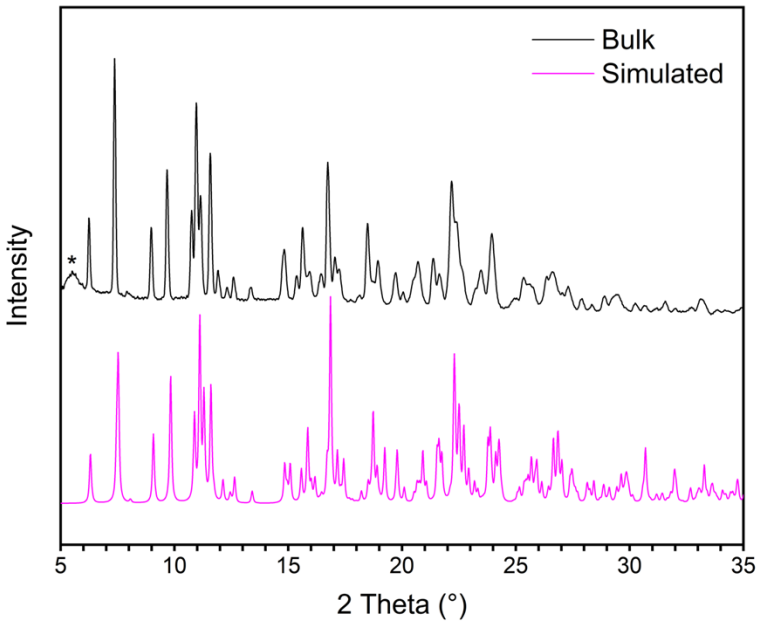

Figure S38: Comparison of Powder XRD pattern (CuKα radiation, λ = 1.5418 Å) from single crystal (simulated) and the bulk powder sample of $Zn(Diclo)_2(biim\text{-}8)$ (*Kapton film).

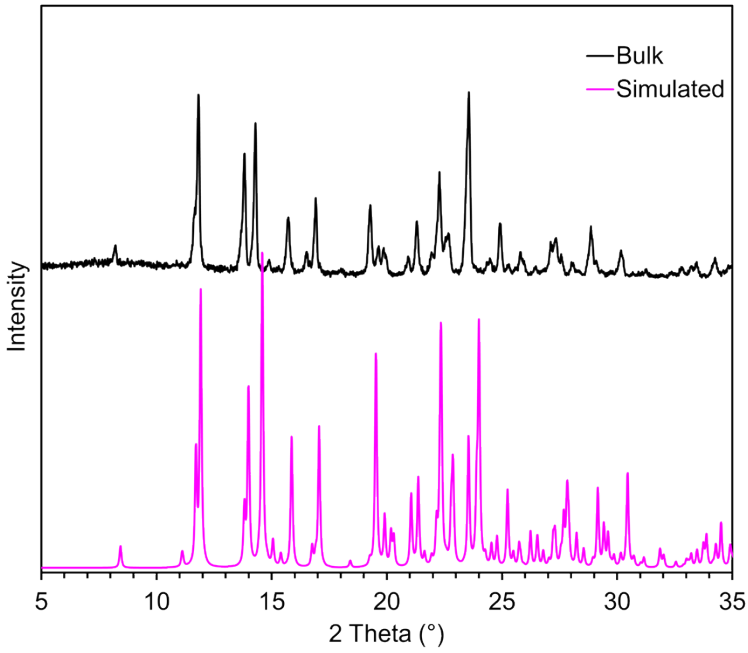

Figure S39: Comparison of Powder XRD pattern (CuKα radiation, λ = 1.5418 Å) from single crystal (simulated) and the bulk powder sample of $Mg(Diclo)_2(biim\text{-}6)(MeOH)_2$.

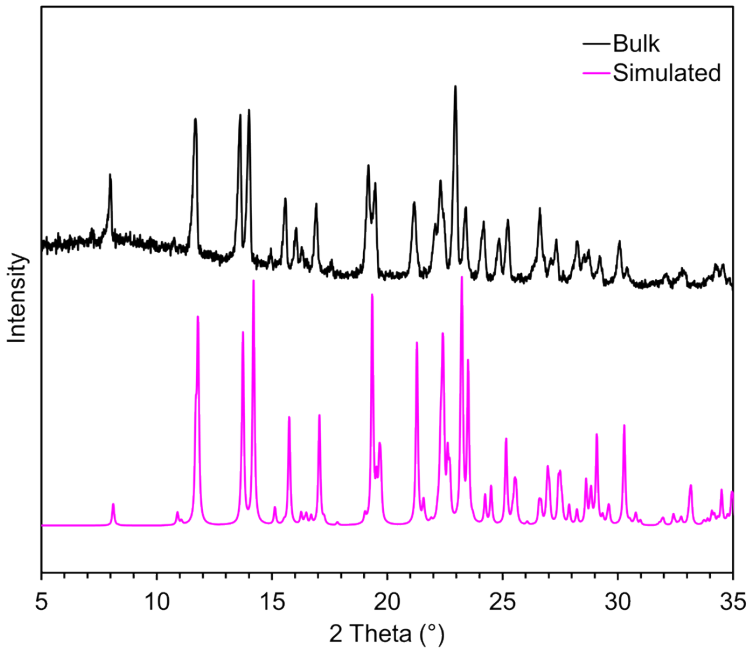

Figure S40: Comparison of Powder XRD pattern (CuKα radiation, λ = 1.5418 Å) from single crystal (simulated) and the bulk powder sample of $Mg(Diclo)_2(biim\text{-}6)(EtOH)_2$.

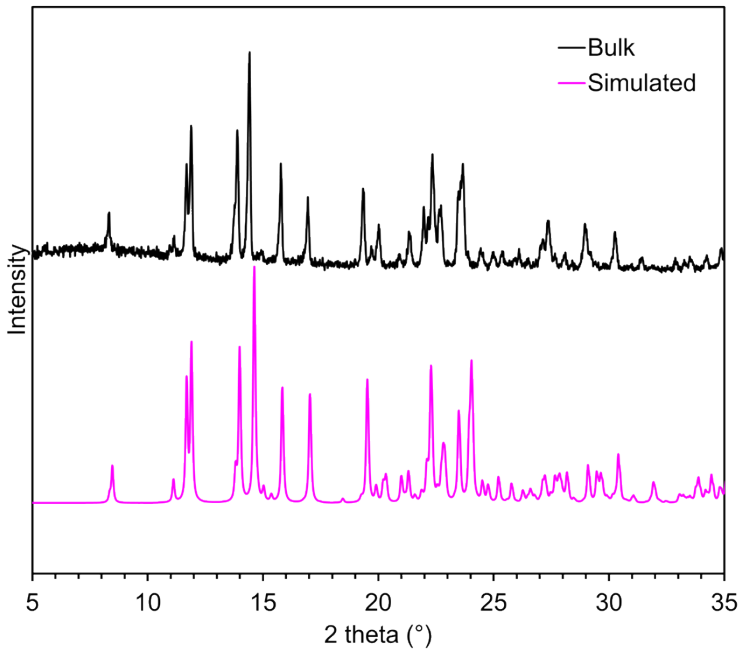

Figure S41: Comparison of Powder XRD pattern (CuKα radiation, λ = 1.5418 Å) from single crystal (simulated) and the bulk powder sample of $Mn(Diclo)_2(biim\text{-}6)(MeOH)_2$.

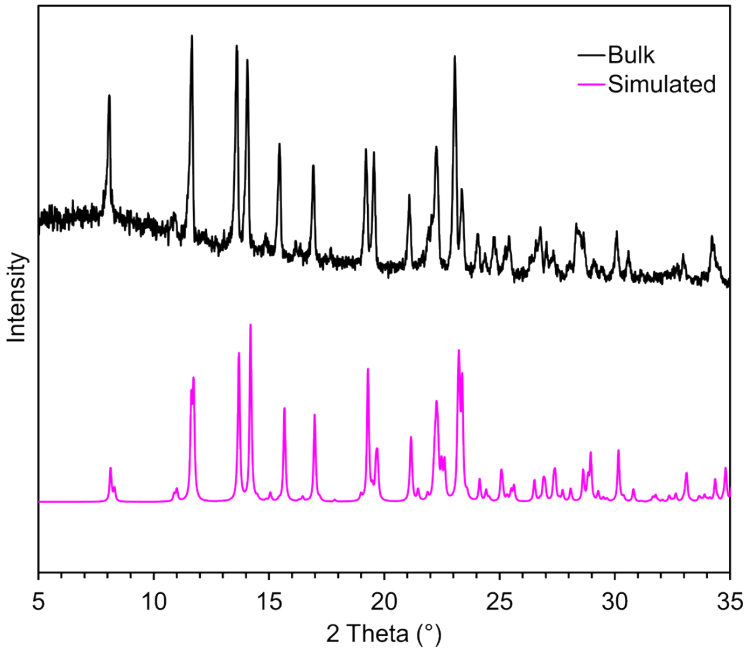

Figure S42: Comparison of Powder XRD pattern (CuKα radiation, λ = 1.5418 Å) from single crystal (simulated) and the bulk powder sample of $Mn(Diclo)_2(biim\text{-}6)(EtOH)_2$.

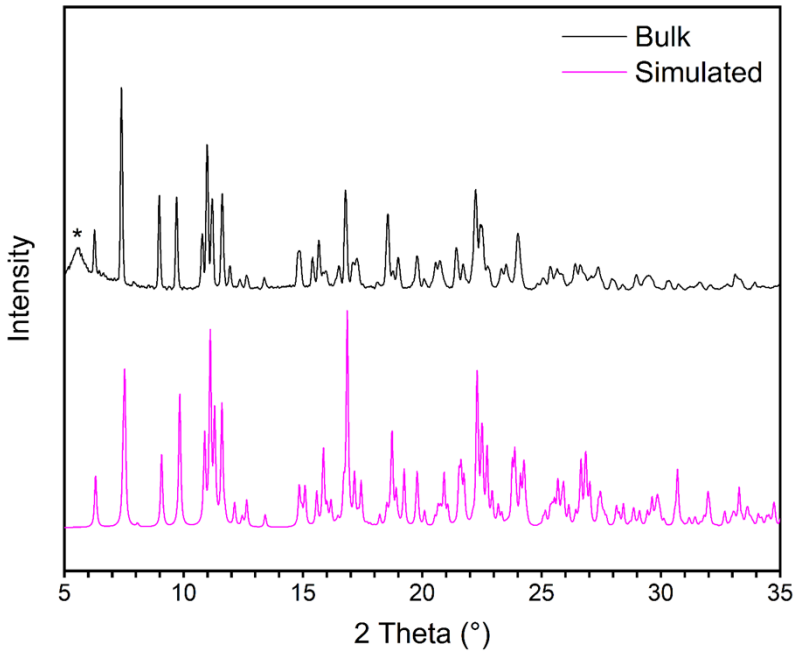

Figure S43: Comparison of Powder XRD pattern (CuKα radiation, λ = 1.5418 Å) from single crystal (simulated) and the bulk powder sample of $Zn(Diclo)_2(biim\text{-}8)$ taken after 1 year.

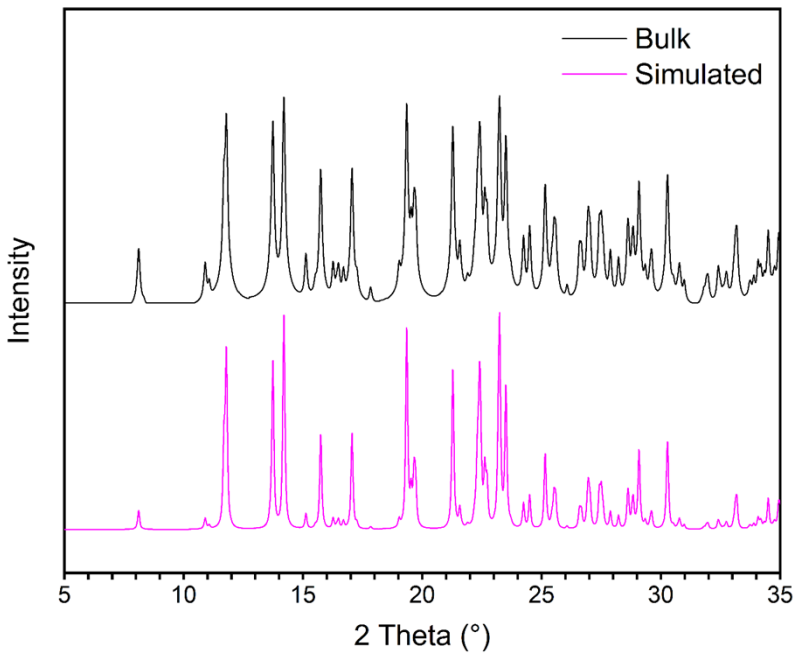

Figure S44: Comparison of Powder XRD pattern (CuKα radiation, λ = 1.5418 Å) from single crystal (simulated) and the bulk powder sample of $Mg(Diclo)_2(biim\text{-}6)(EtOH)_2$ taken after 1 year.

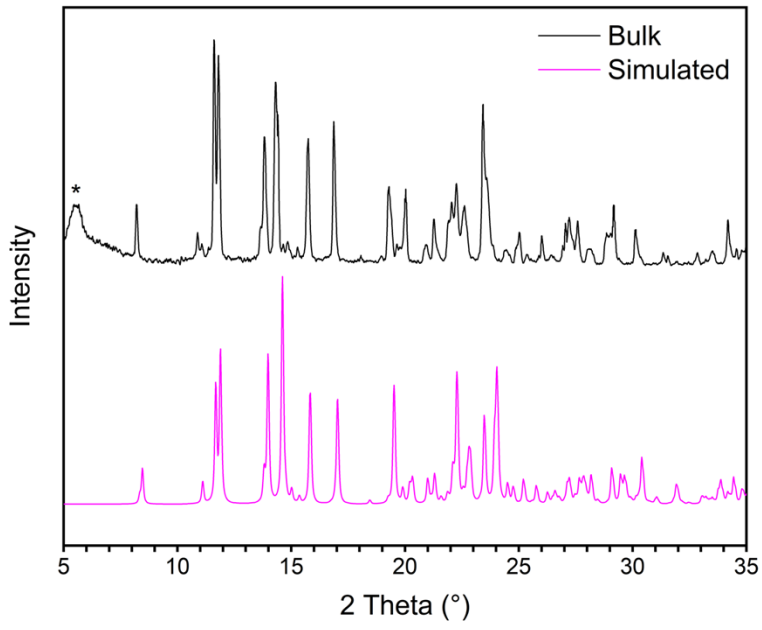

Figure S45: Comparison of Powder XRD pattern (CuKα radiation, λ = 1.5418 Å) from single crystal (simulated) and the bulk powder sample of $Mn(Diclo)_2(biim\text{-}6)(MeOH)_2$ taken after 1 year (*Kapton film).

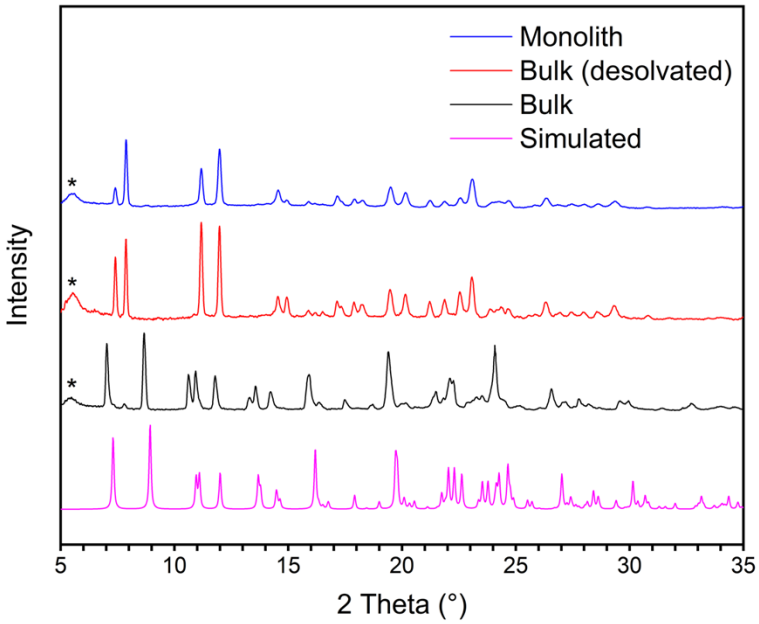

Figure S46: Comparison of Powder XRD pattern (CuKα radiation, λ = 1.5418 Å) from single crystal (simulated), the bulk powder sample of $Cu(Diclo)_2(biim\text{-}6)\cdot(MeOH)_2$, the bulk powder sample desolvated ($Cu(Diclo)_2(biim\text{-}6)'$), and the monolith (*Kapton film).

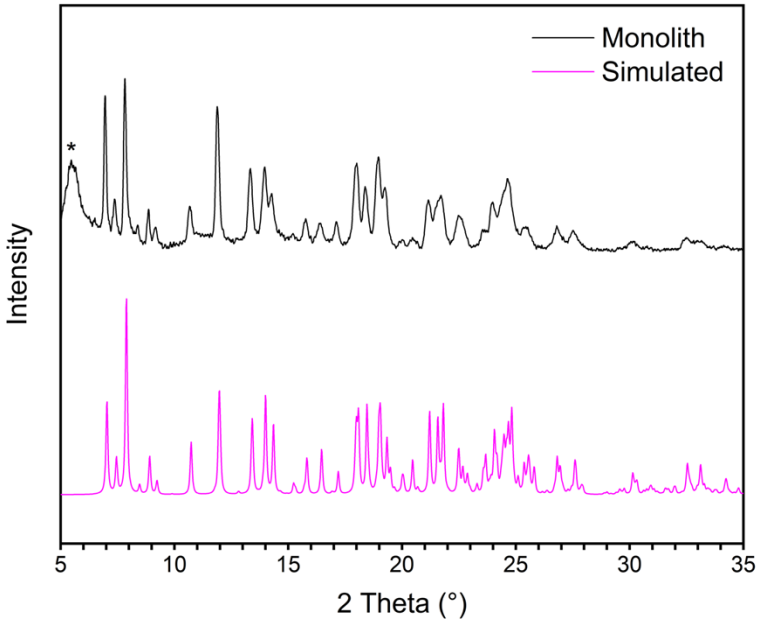

Figure S47: Comparison of Powder XRD pattern (CuKα radiation, λ = 1.5418 Å) from single crystal (simulated) and the monolith of $Zn(Diclo)_2(biim\text{-}6)\cdot(EtOH)$ (*Kapton film).

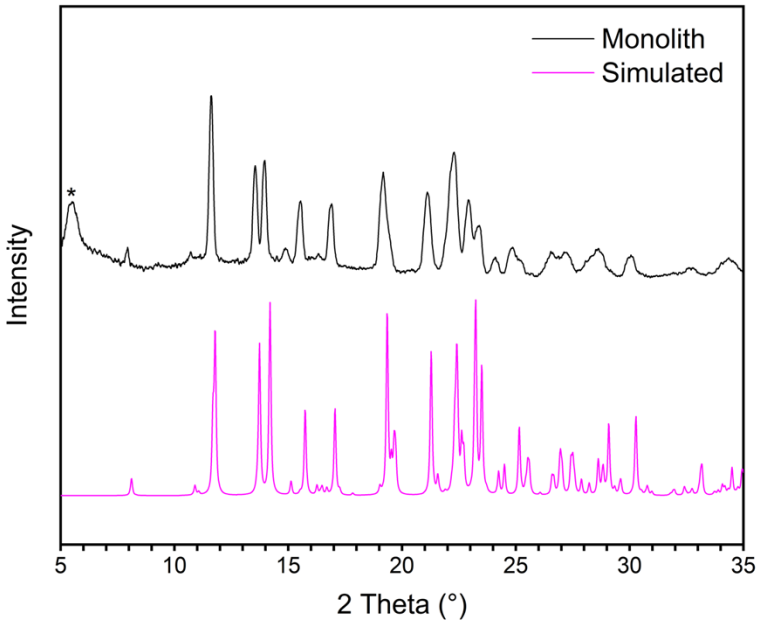

Figure S48: Comparison of Powder XRD pattern (CuKα radiation, λ = 1.5418 Å) from single crystal (simulated) and the monolith of $Mg(Diclo)_2(biim\text{-}6)(EtOH)_2$ (*Kapton film).

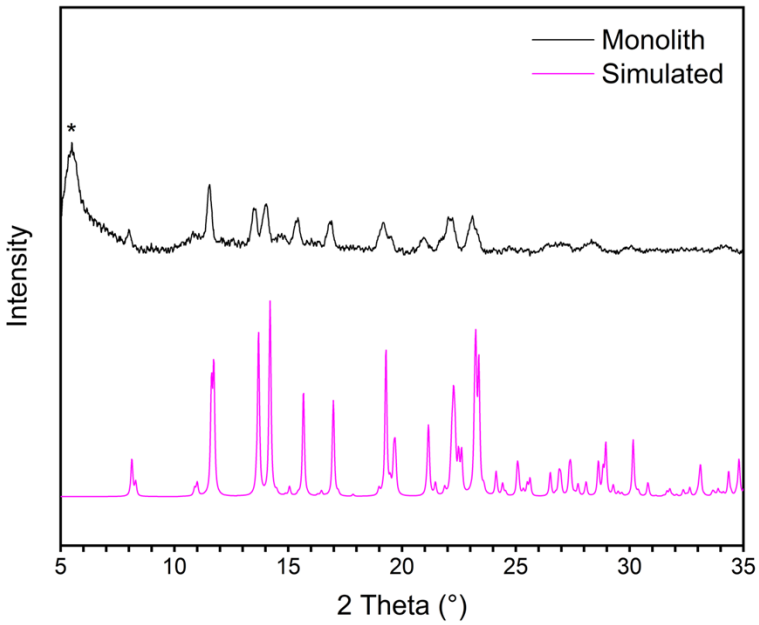

Figure S49: Comparison of Powder XRD pattern (CuKα radiation, λ = 1.5418 Å) from single crystal (simulated) and the monolith of $Mn(Diclo)_2(biim\text{-}6)(EtOH)_2$ (*Kapton film).

4. Thermogravimetric Analysis

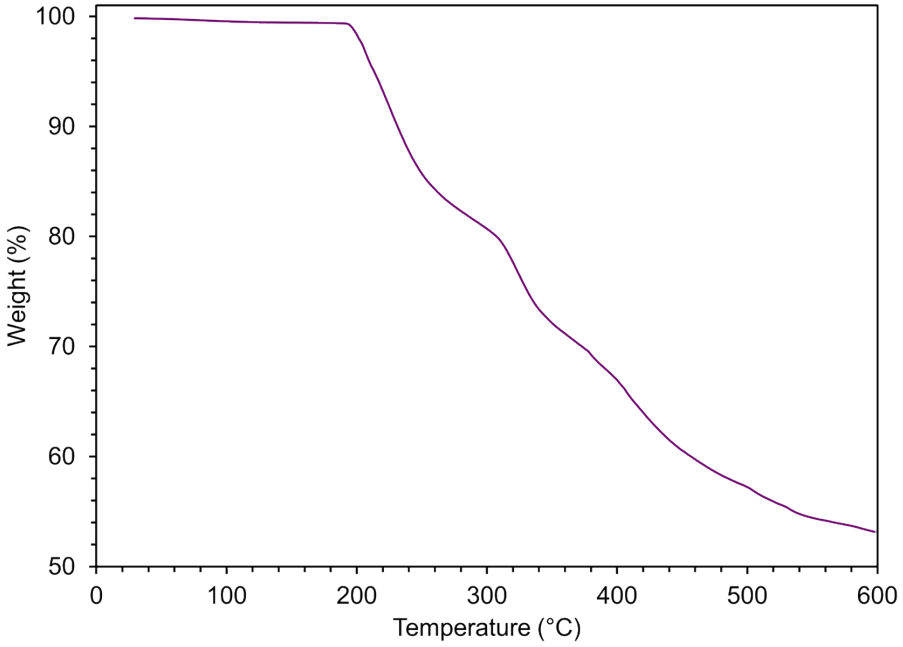

Figure S50: Thermogravimetric analysis $Cu(Diclo)_2(biim\text{-}5)$.

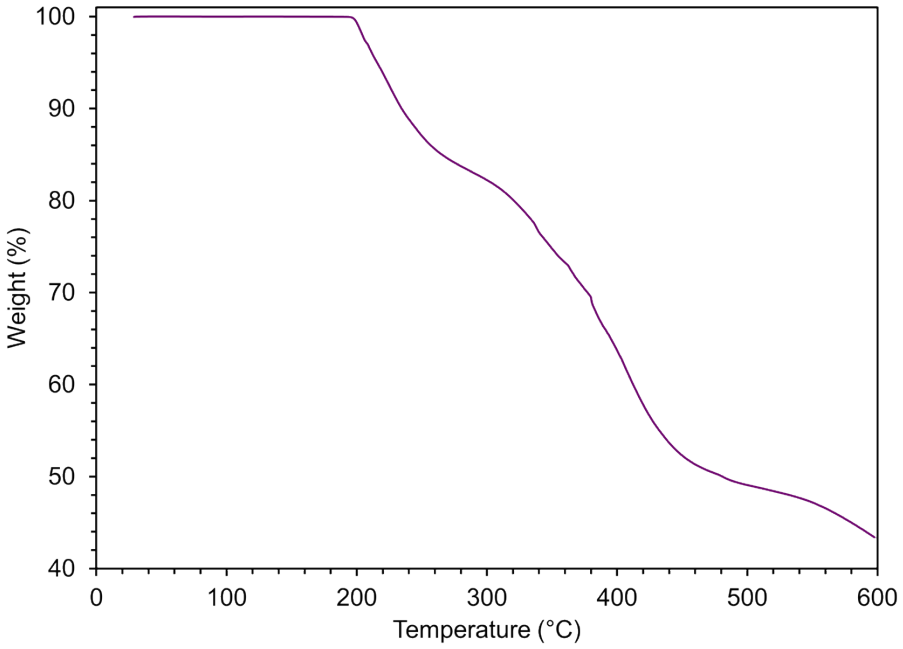

Figure S51: Thermogravimetric analysis of desolvated $Cu(Diclo)_2(biim\text{-}6)'$.

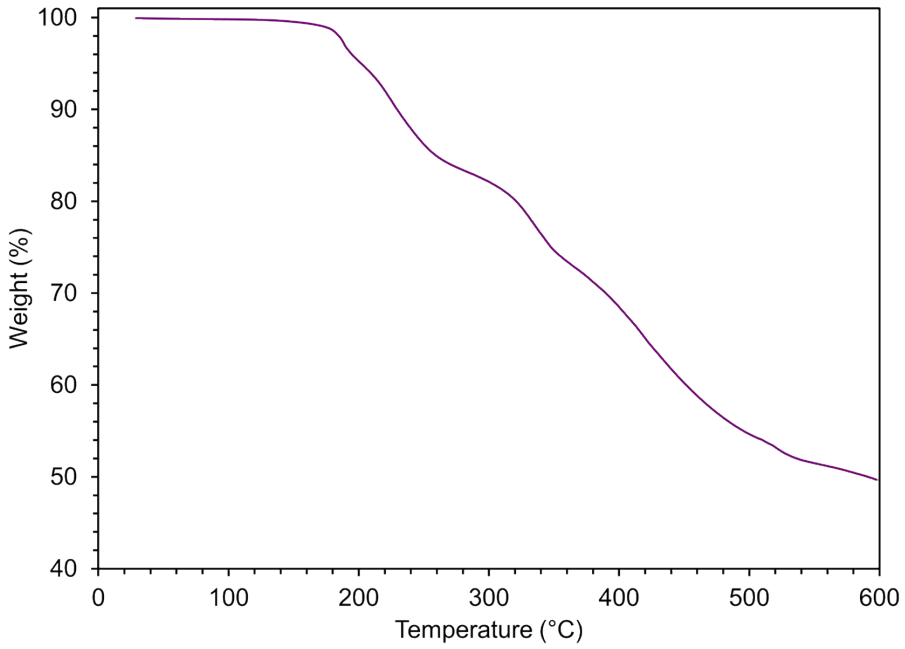

Figure S52: Thermogravimetric analysis of $Cu(Diclo)_2(biim\text{-}8)\cdot(MeOH)_2$.

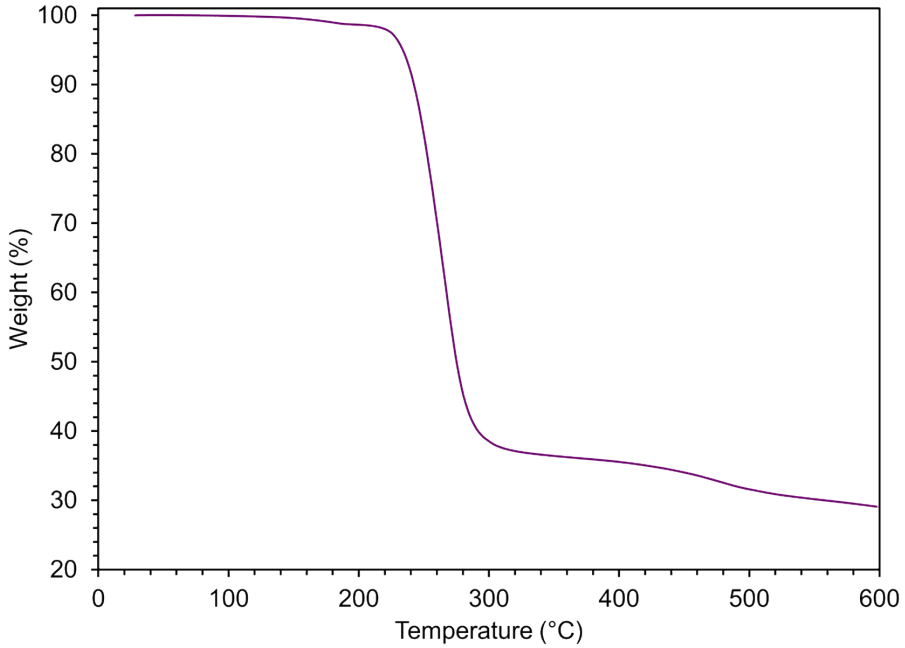

Figure S53: Thermogravimetric analysis $Zn(Diclo)_2(biim\text{-}5)$.

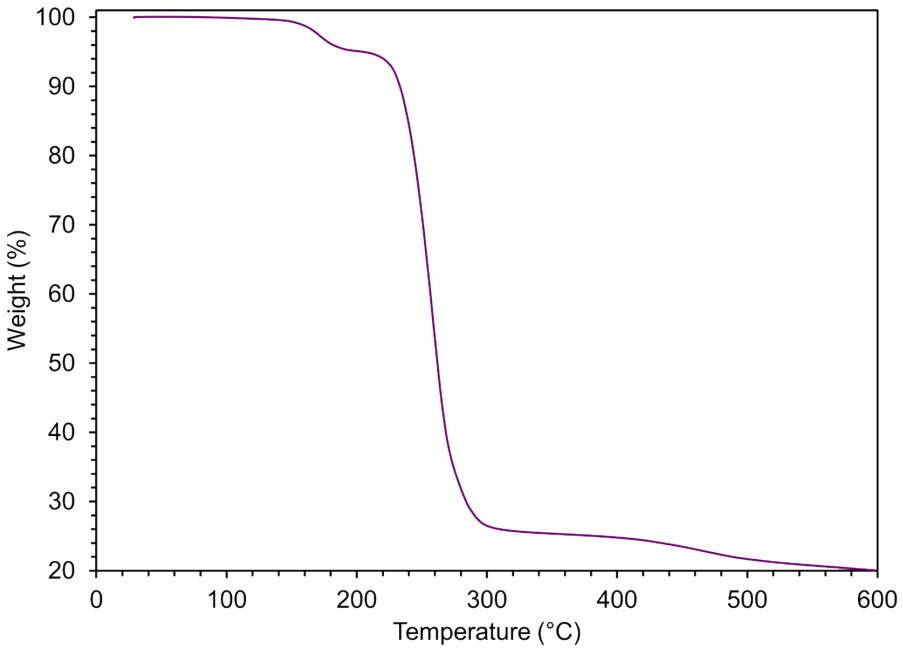

Figure S54: Thermogravimetric analysis $Zn(Diclo)_2(biim\text{-}6)\cdot(MeOH)$.

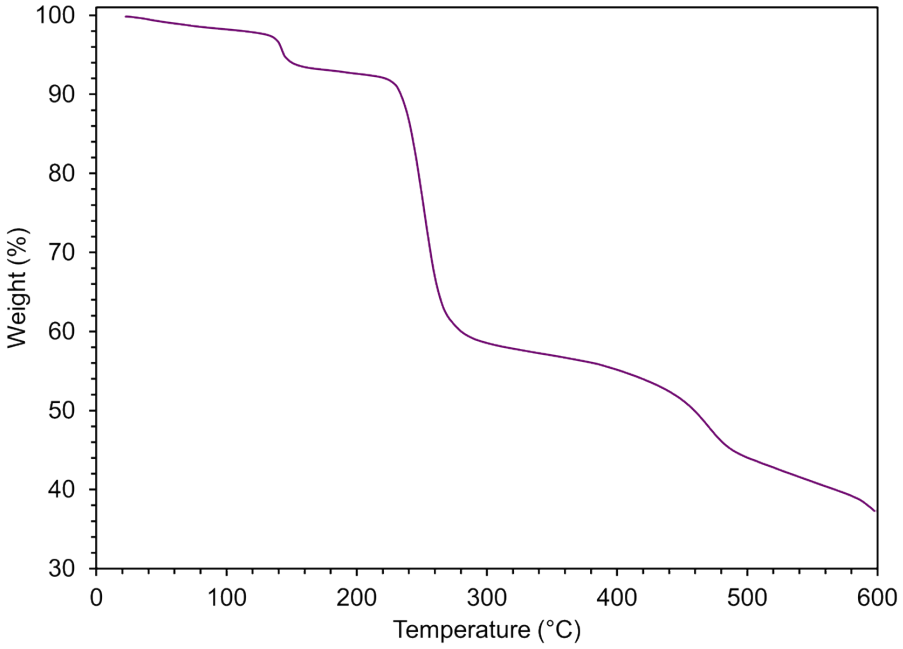

Figure S55: Thermogravimetric analysis of $Zn(Diclo)_2(biim\text{-}6)\cdot(EtOH)$.

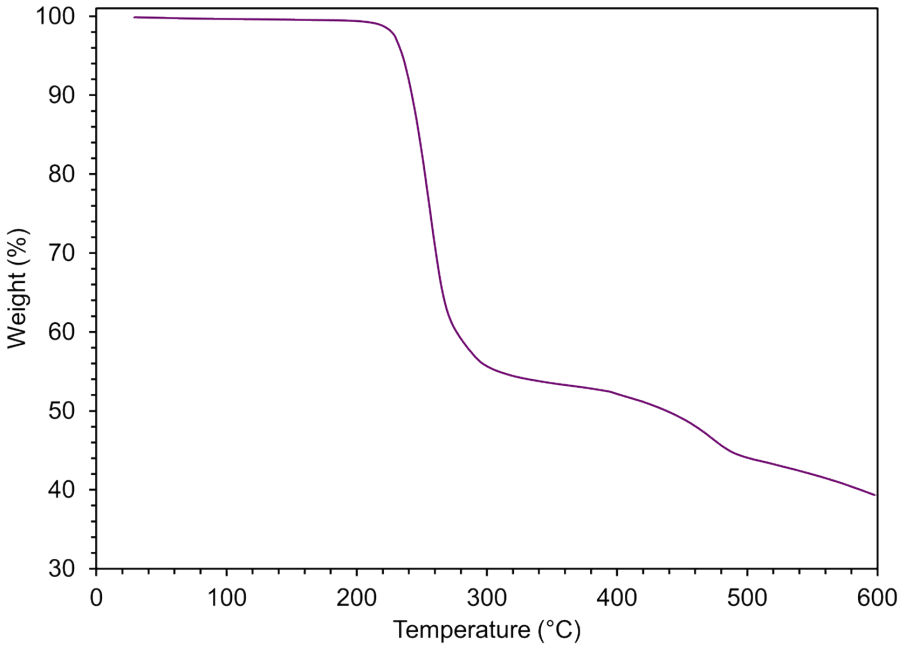

Figure S56: Thermogravimetric analysis of $Zn(Diclo)_2(biim\text{-}8)$.

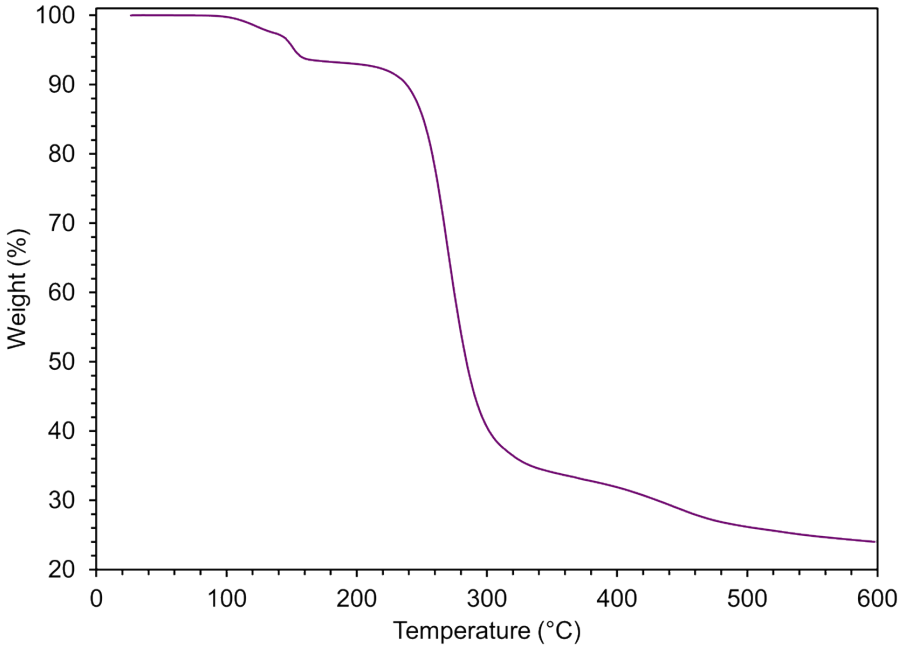

Figure S57: Thermogravimetric analysis of $Mg(Diclo)_2(biim\text{-}6)(MeOH)_2$.

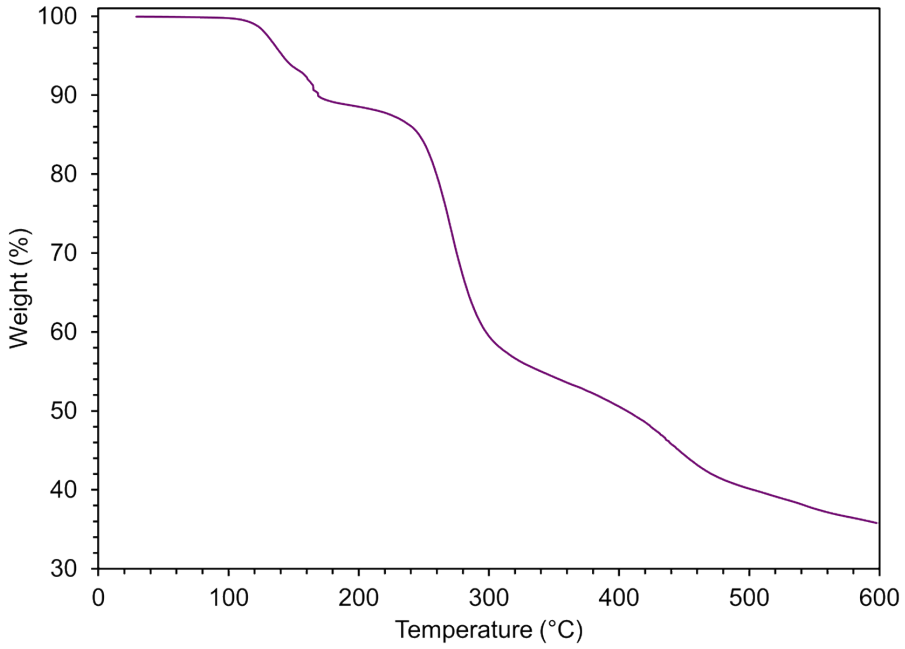

Figure S58: Thermogravimetric analysis of $Mg(Diclo)_2(biim\text{-}6)(EtOH)_2$.

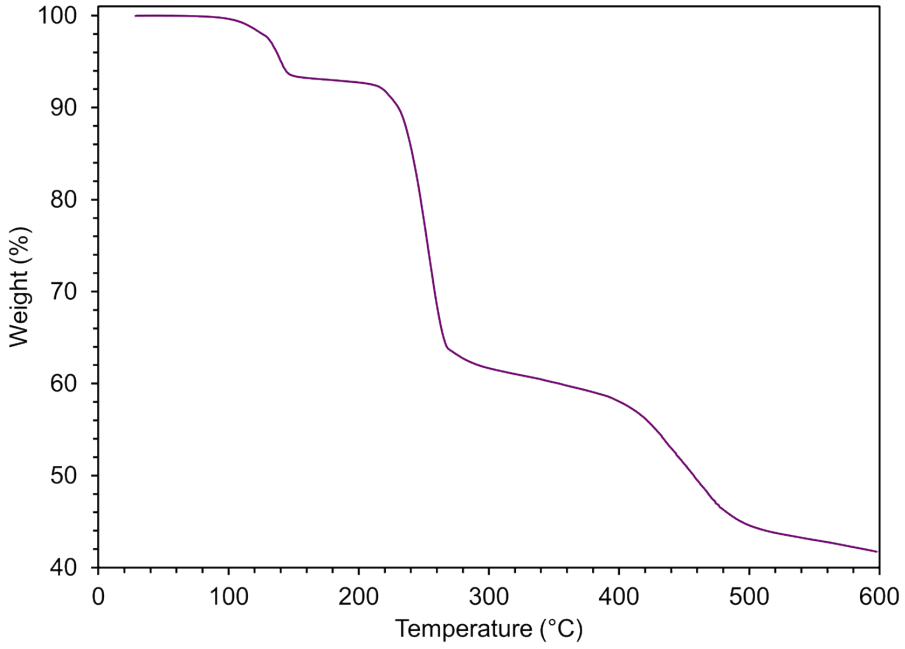

Figure S59: Thermogravimetric analysis of $Mn(Diclo)_2(biim\text{-}6)(MeOH)_2$.

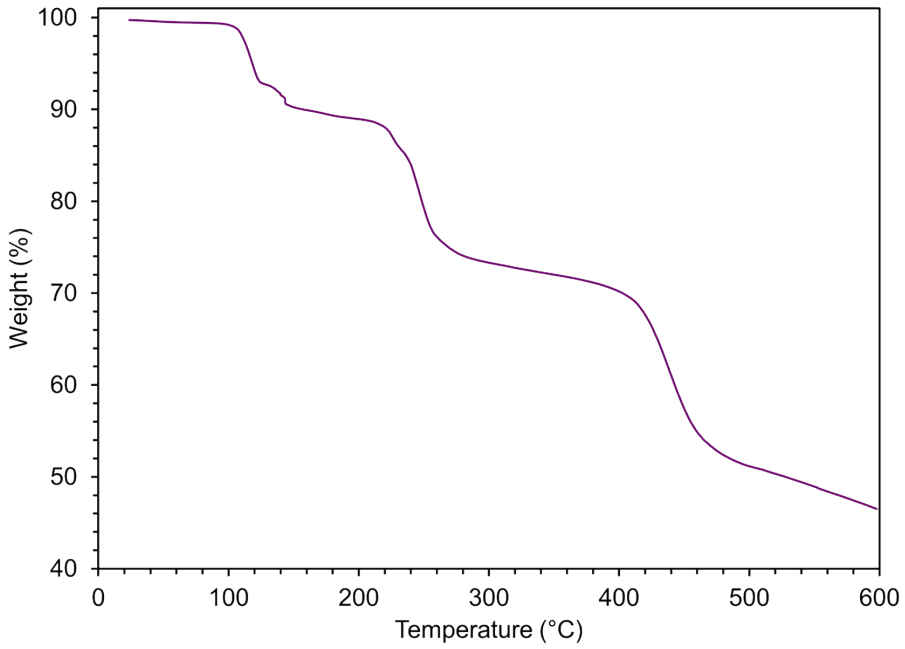

Figure S60: Thermogravimetric analysis of $Mn(Diclo)_2(biim\text{-}6)(EtOH)_2$.

5. Dissolution Data

5.1 Calibration Curves

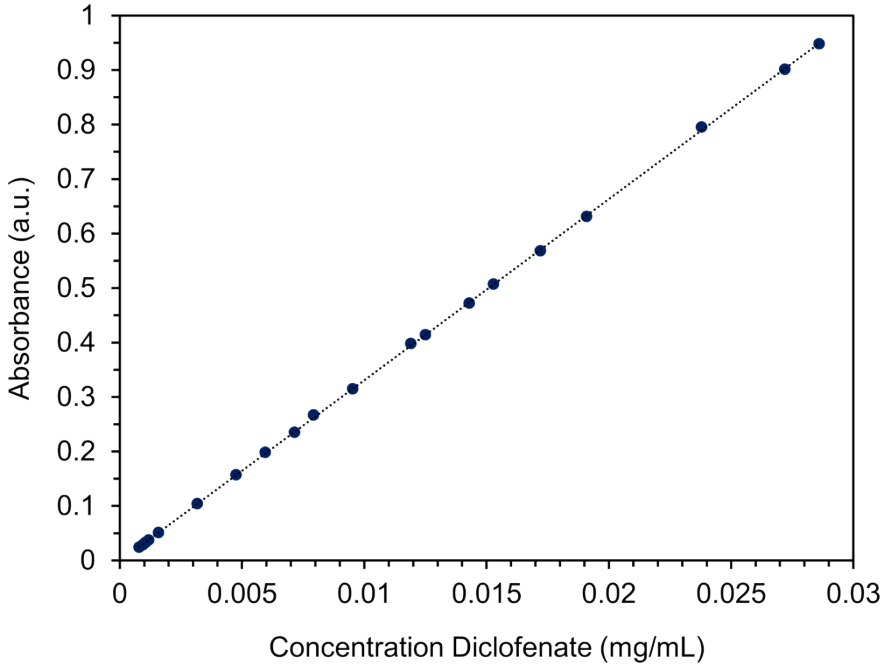

Figure S61: Calibration curve for sodium Diclofenac in 0.05 M phosphate buffer, pH 6.8 y=33.248x-0.0015, R^2 = 0.9999

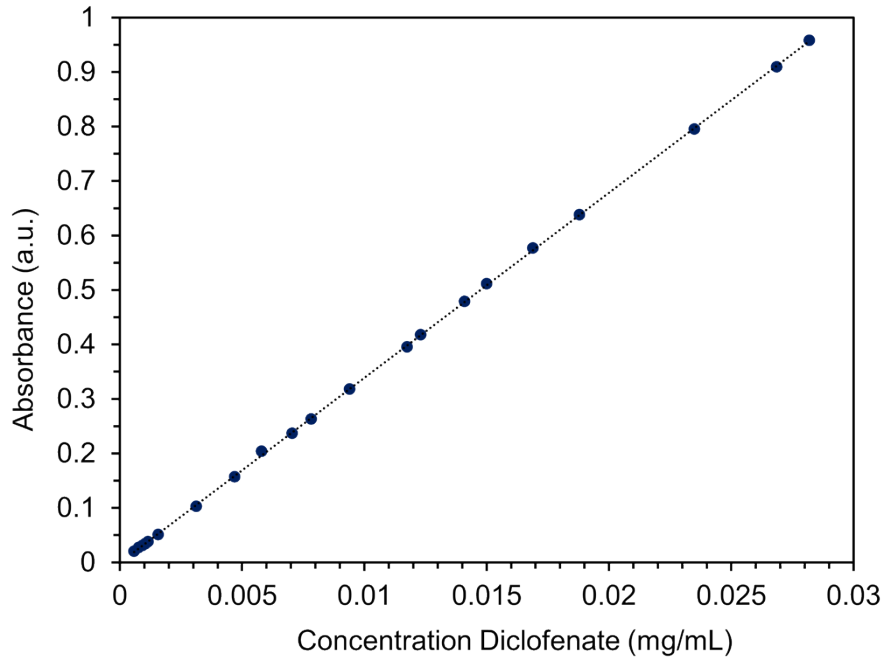

Figure S62: Calibration curve for sodium Diclofenac in 0.05 M phosphate buffer, pH 6.8 with 0.05% EDTA. y=33.955x-0.0007, R^2 = 0.9999.

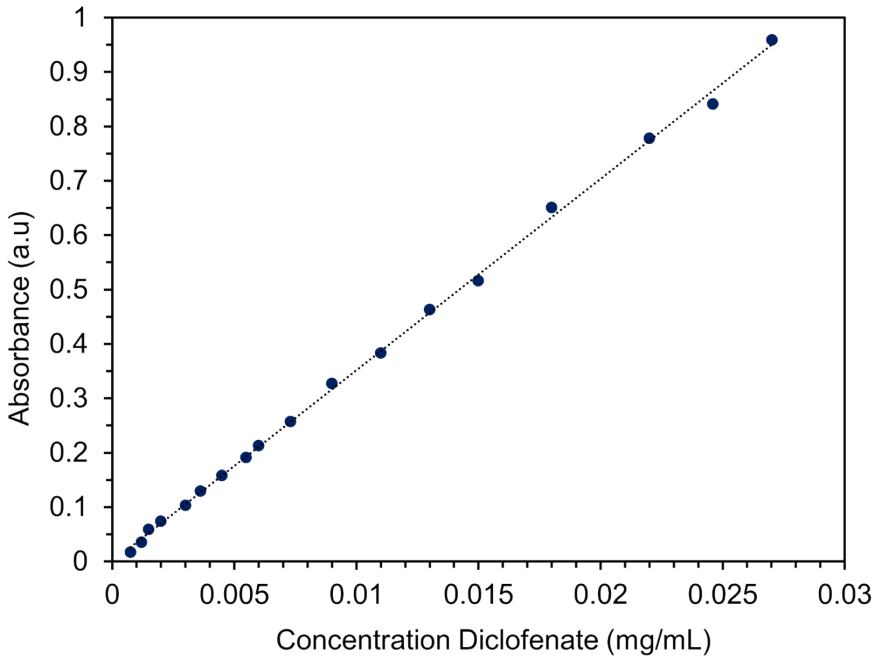

Figure S63: Calibration curve for sodium Diclofenac in 0.01 M citrate buffer, pH 5.5. y=35.19x-0.0002, $R^2 = 0.9990$.

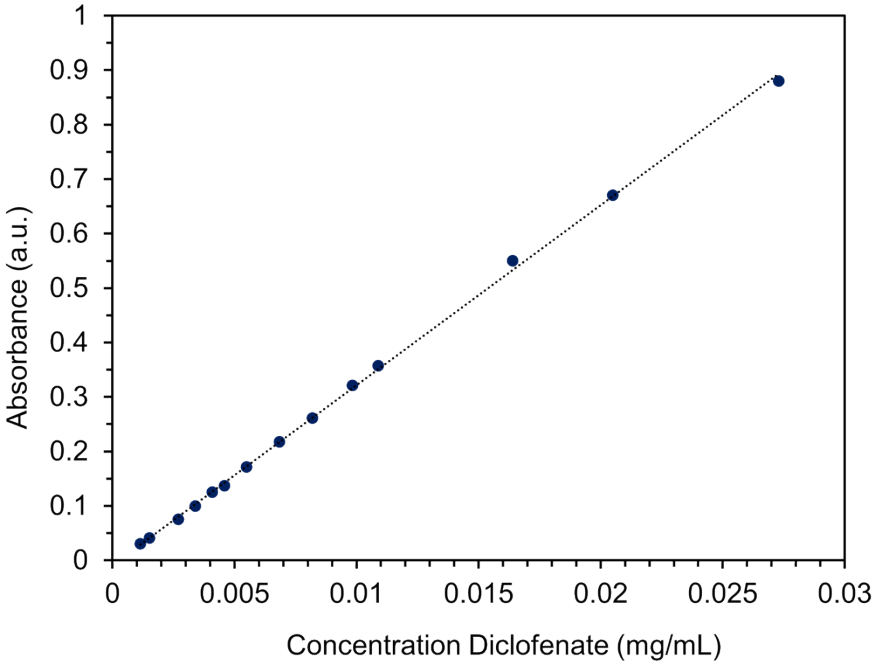

Figure S64: Calibration curve for sodium Diclofenac in 0.01 M citrate buffer, pH 5.5 with 0.05% SDS. y=33.059x-0.0093, $R^2 = 0.9993$.

5.2 Tablet Dissolution

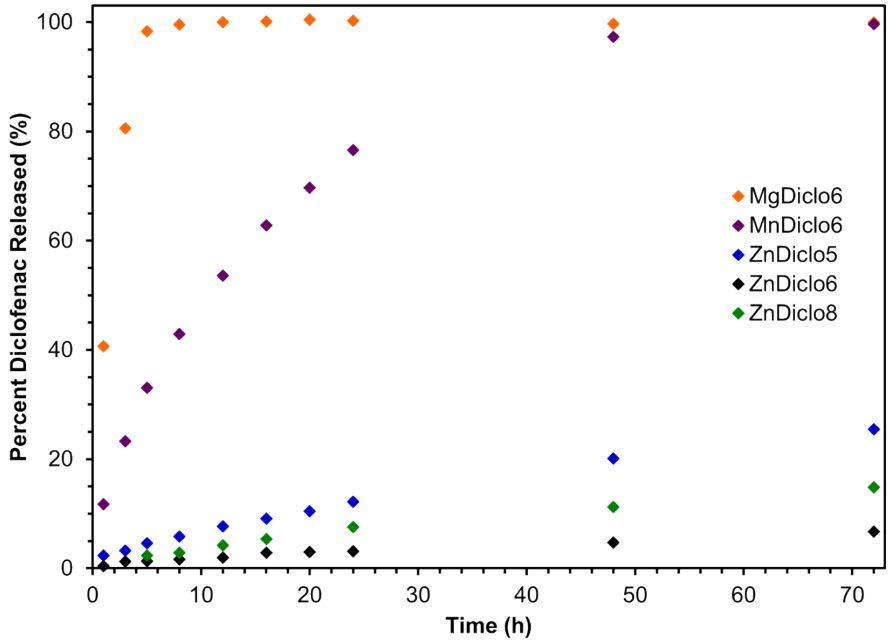

Figure S65: The release of Diclofenac from imidazole-based therapeutic coordination polymers over 72 h in 0.05 M phosphate buffer, pH 6.8.

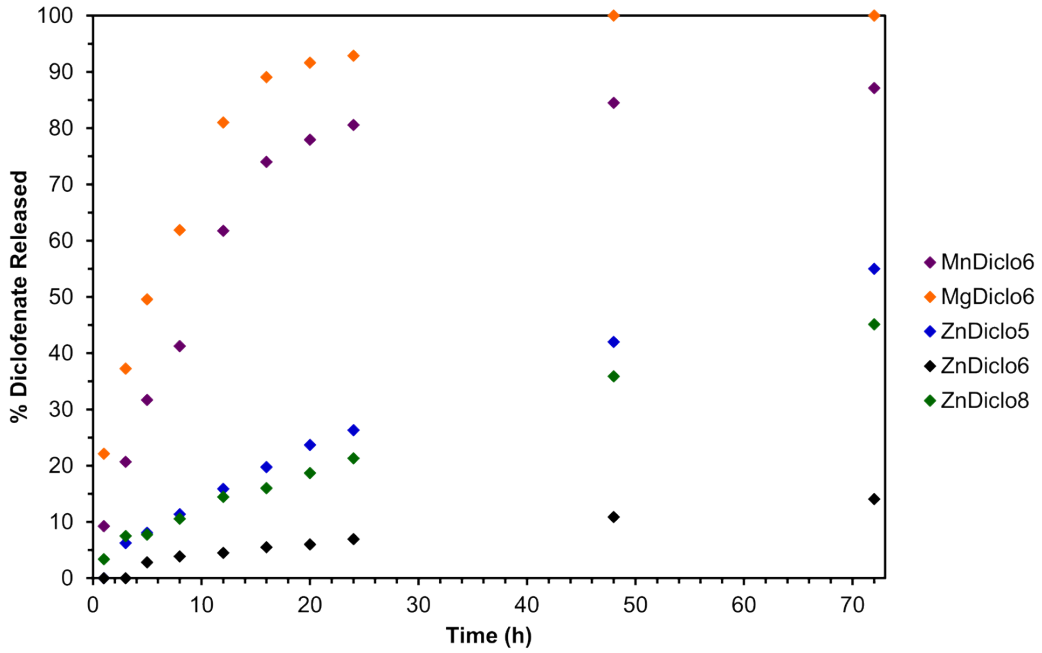

Figure S66: The release of Diclofenac from imidazole-based therapeutic coordination polymers over 72 h in 0.01 M citrate buffer, pH 5.5.

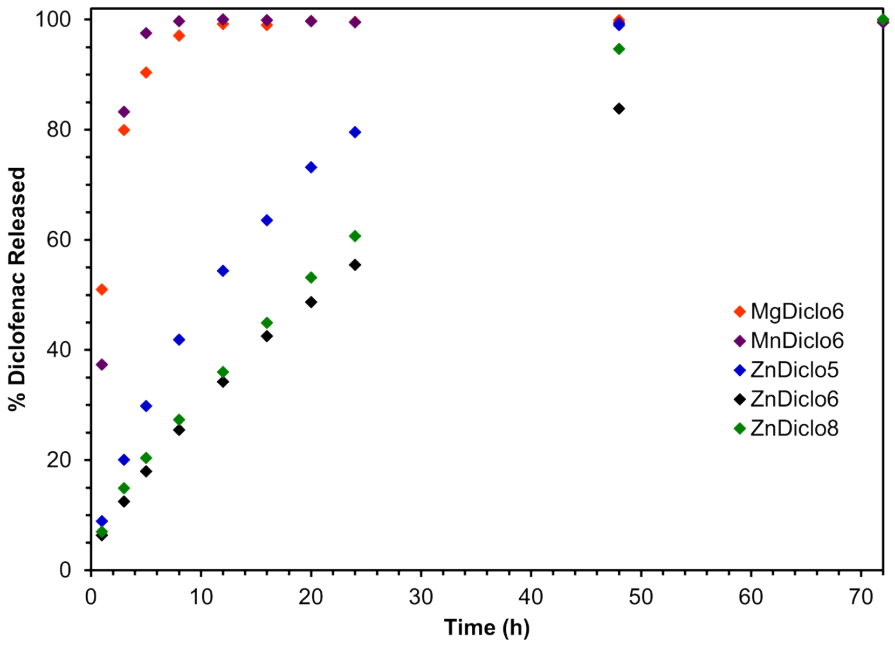

Figure S67: The release of Diclofenac from imidazole-based therapeutic coordination polymers over 72 h in 0.01 M citrate buffer, pH 5.5 with 0.05% SDS.

.

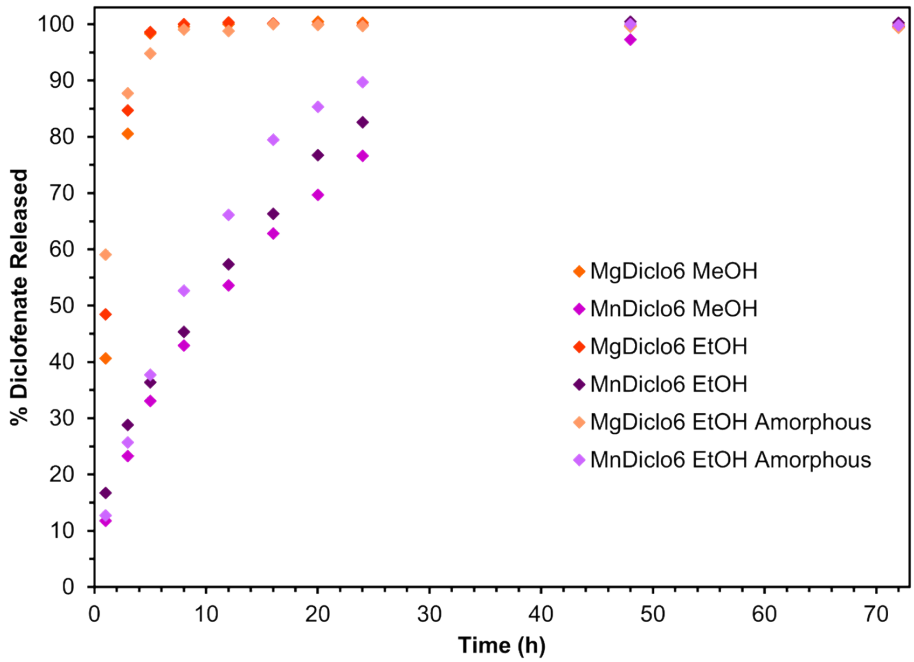

Figure S68: The release of Diclofenac from Mn and Mg therapeutic coordination polymers prepared in methanol, ethanol, and amorphized over 72 h in 0.05 M phosphate buffer, pH 6.8.

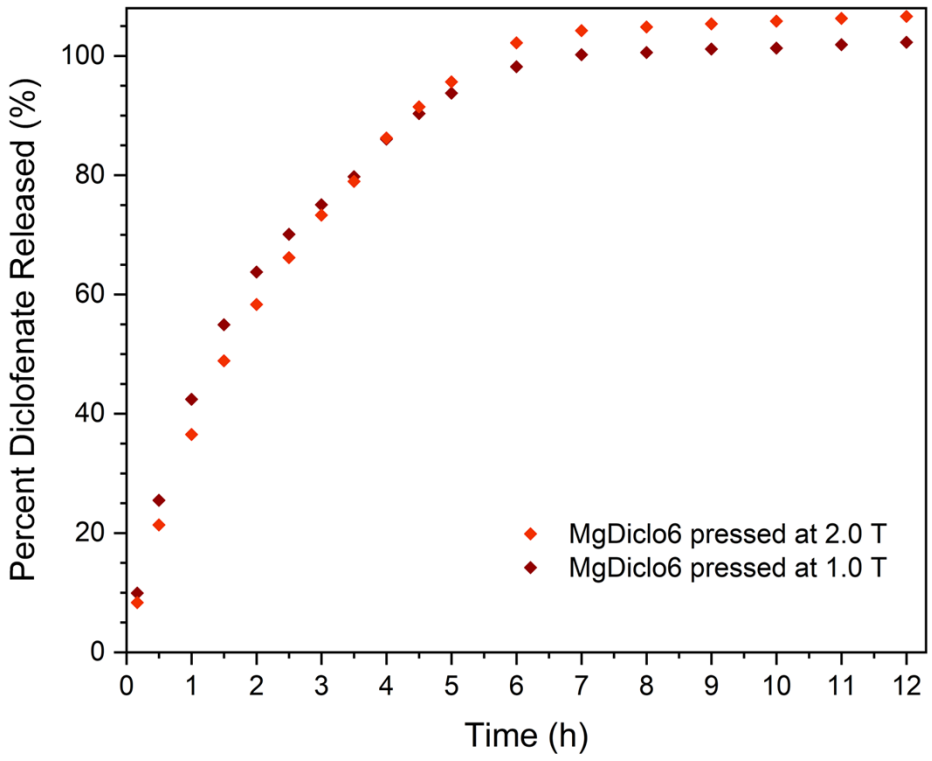

Figure S69: The release of Diclofenac from $Mg(Diclo)_2(biim\text{-}6)(EtOH)_2$ pressed into monoliths of 2 different pressures over 12 h in 0.05M phosphate buffer, pH 6.8.

5.3 Intrinsic Dissolution Rates

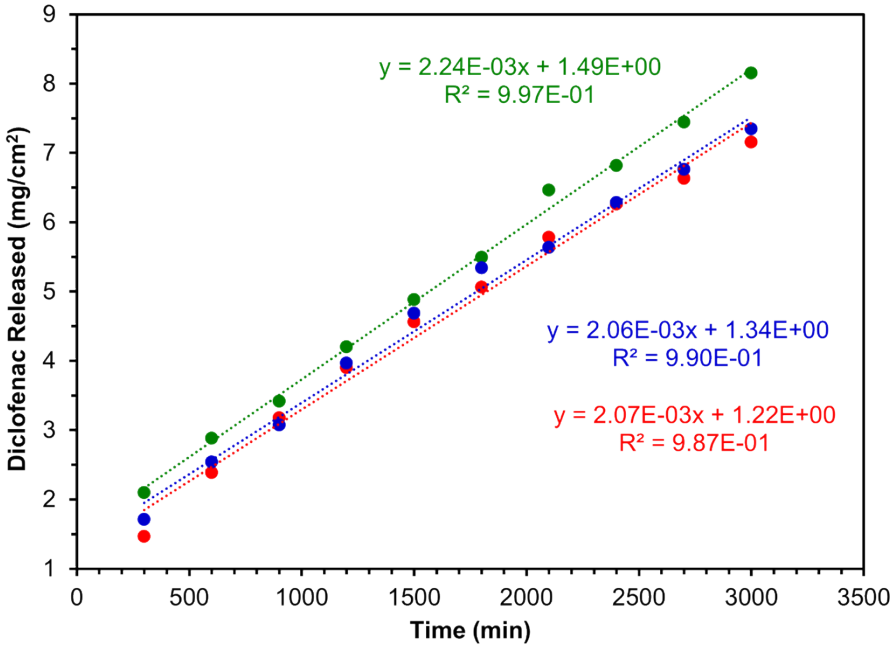

Figure S70*:* Intrinsic dissolution replicates of $Zn(Diclo)_2(biim\text{-}5)$ in 0.05 M phosphate buffer, pH 6.8. Linear fitting of data corresponds to the intrinsic dissolution rate. Linear equation and corresponding R^2 values are shown in colors to match data sets.

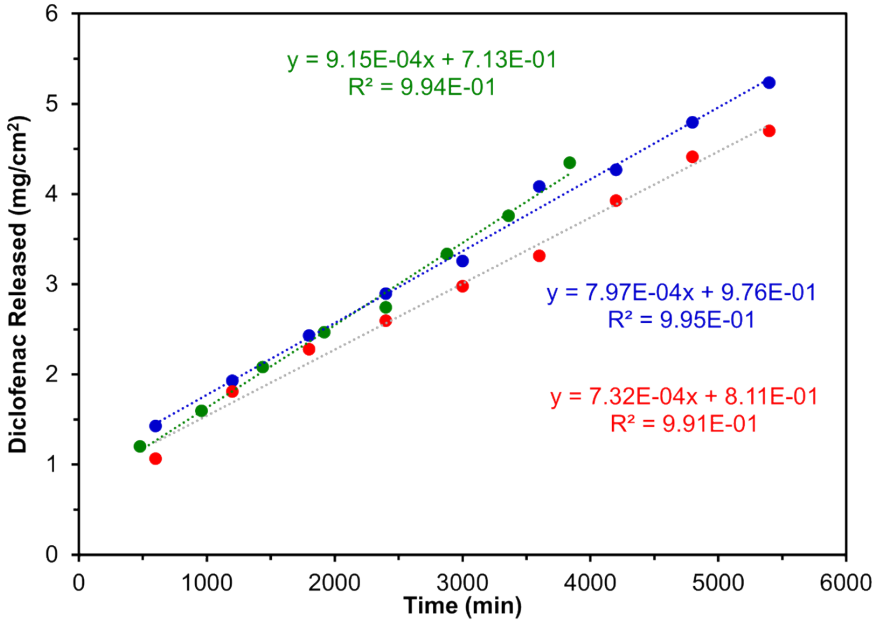

Figure S71: Intrinsic dissolution replicates of $Zn(Diclo)_2(biim\text{-}6)\cdot(EtOH)$ in 0.05 M phosphate buffer, pH 6.8. Linear fitting of data corresponds to the intrinsic dissolution rate. Linear equation and corresponding R^2 values are shown in colors to match data sets.

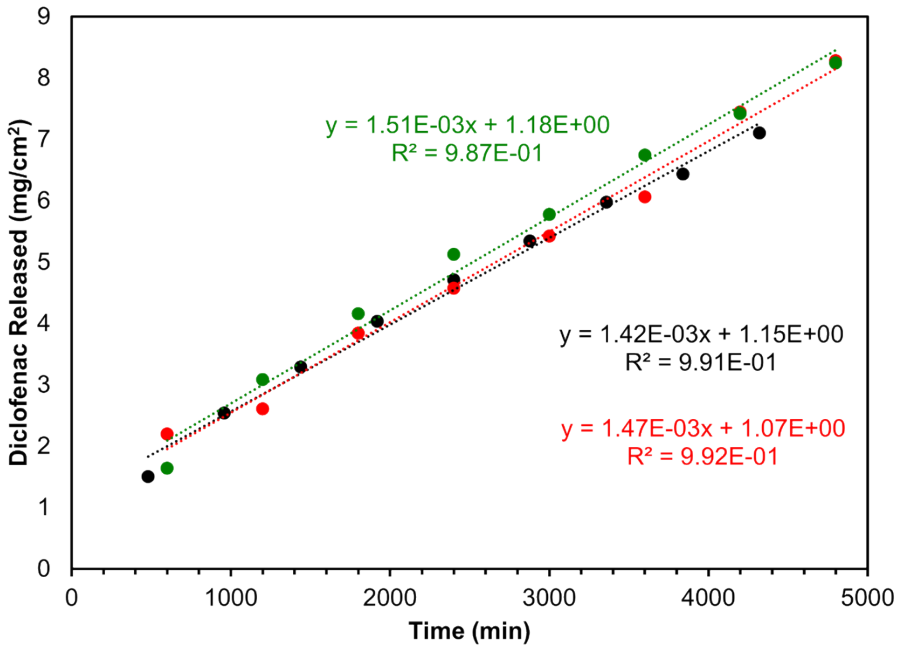

Figure S72: Intrinsic dissolution replicates of $Zn(Diclo)_2(biim\text{-}8)$ in 0.05 M phosphate buffer, pH 6.8. Linear fitting of data corresponds to the intrinsic dissolution rate. Linear equation and corresponding R^2 values are shown in colors to match data sets.

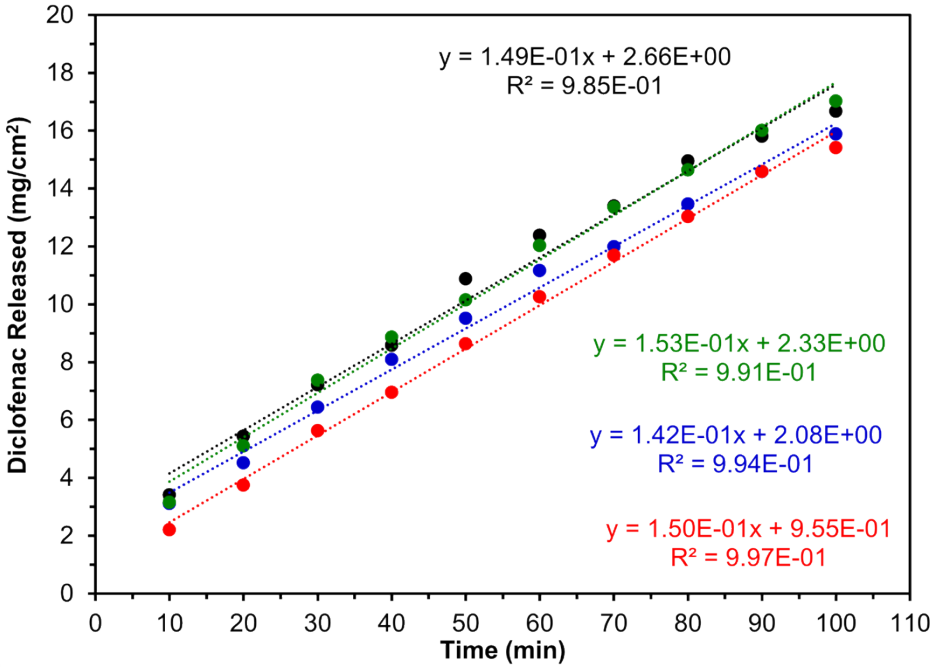

Figure S73: Intrinsic dissolution replicates of $Mg(Diclo)_2(biim\text{-}6)(EtOH)_2$ in 0.05 M phosphate buffer, pH 6.8. Linear fitting of data corresponds to the intrinsic dissolution rate. Linear equation and corresponding R^2 values are shown in colors to match data sets.

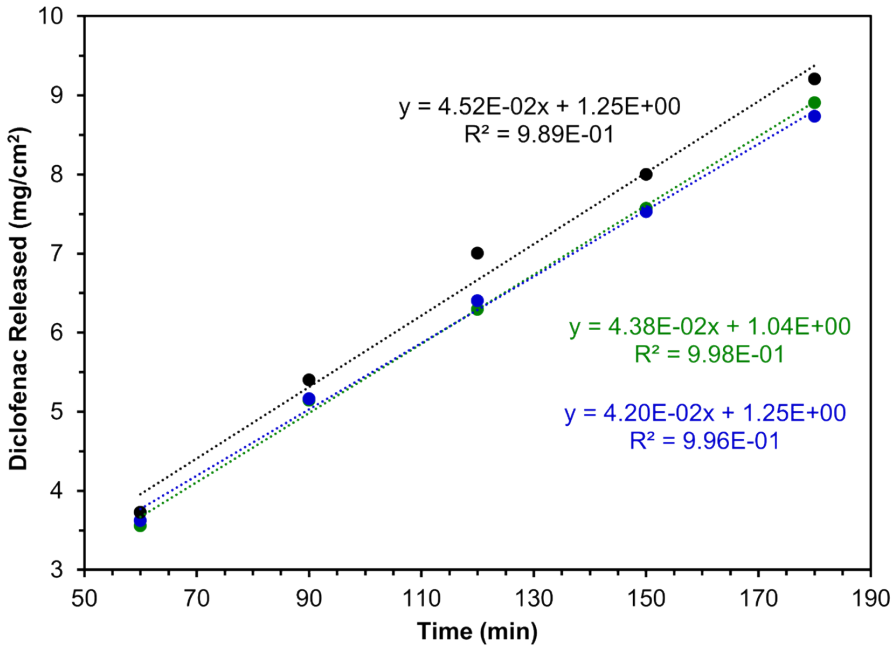

Figure S74*:* Intrinsic dissolution replicates of $Mn(Diclo)_2(biim\text{-}6)(EtOH)_2$ in 0.05 M phosphate buffer, pH 6.8. Linear fitting of data corresponds to the intrinsic dissolution rate. Linear equation and corresponding R^2 values are shown in colors to match data sets.

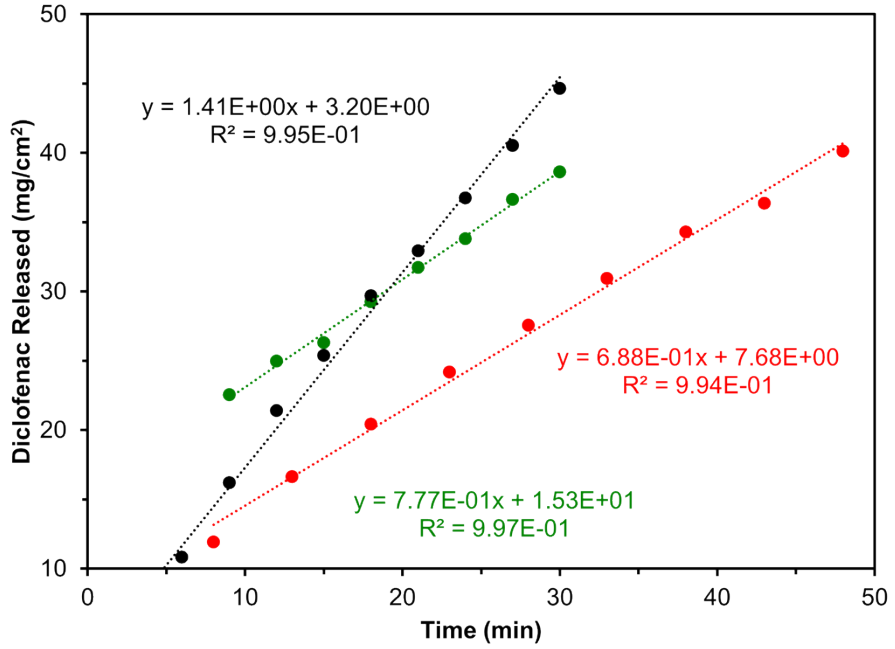

Figure S75: Intrinsic dissolution replicates of sodium Diclofenac in 0.05 M phosphate buffer, pH 6.8. Linear fitting of data corresponds to the intrinsic dissolution rate. Linear equation and corresponding R^2 values are shown in colors to match data sets.

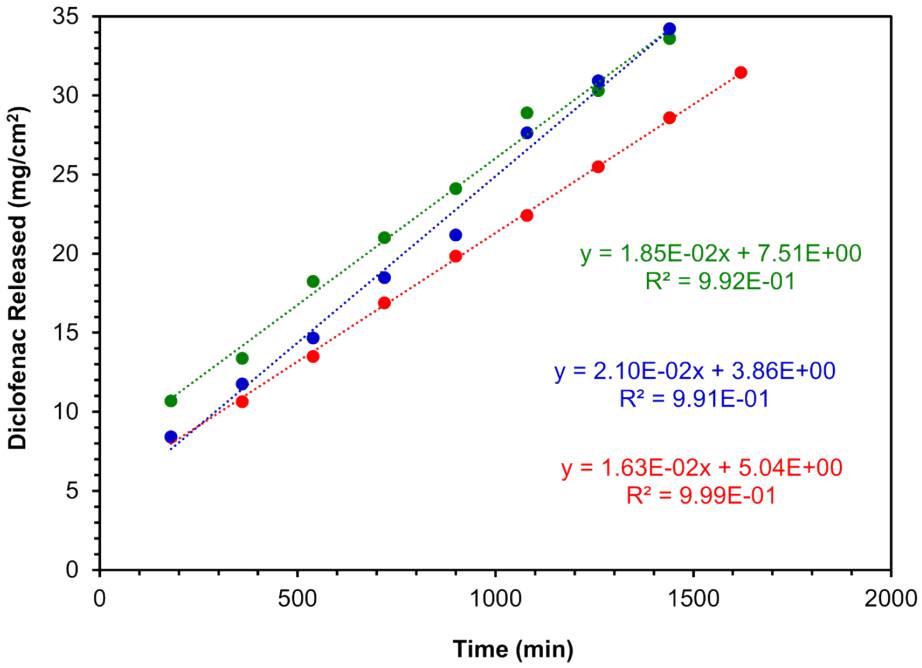

Figure S76: Intrinsic dissolution replicates of $Zn(Diclo)_2(biim\text{-}5)$ in 0.05 M phosphate buffer, pH 6.8 with 0.05% EDTA. Linear fitting of data corresponds to the intrinsic dissolution rate. Linear equation and corresponding R^2 values are shown in colors to match data sets.

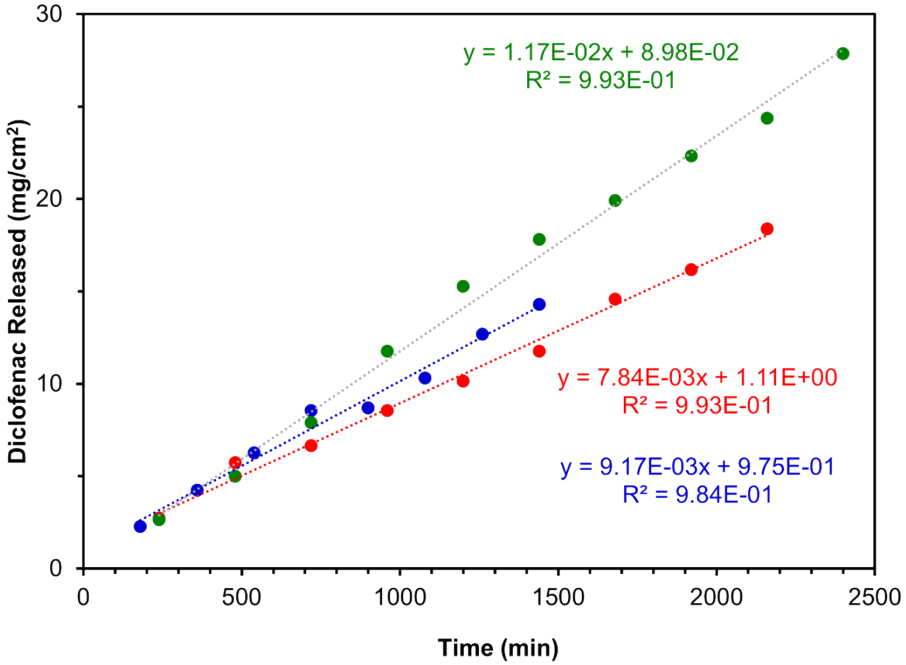

Figure S77: Intrinsic dissolution replicates of $Zn(Diclo)_2(biim\text{-}6)\cdot(EtOH)$ in 0.05 M phosphate buffer, pH 6.8 with 0.05% EDTA. Linear fitting of data corresponds to the intrinsic dissolution rate. Linear equation and corresponding R^2 values are shown in colors to match data sets.

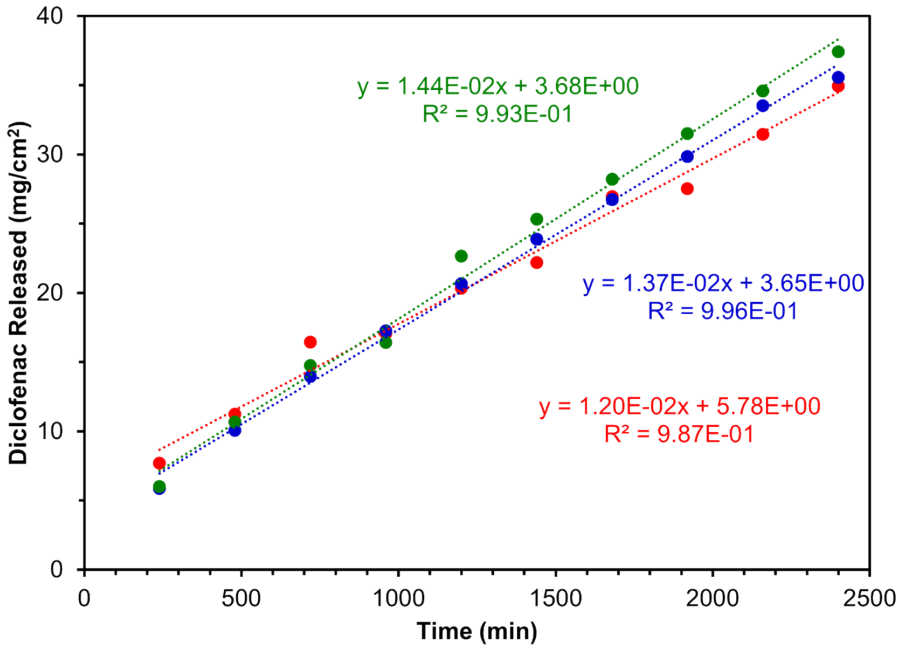

Figure S78: Intrinsic dissolution replicates of $Zn(Diclo)_2(biim\text{-}8)$ in 0.05 M phosphate buffer, pH 6.8 with 0.05% EDTA. Linear fitting of data corresponds to the intrinsic dissolution rate. Linear equation and corresponding R^2 values are shown in colors to match data sets.

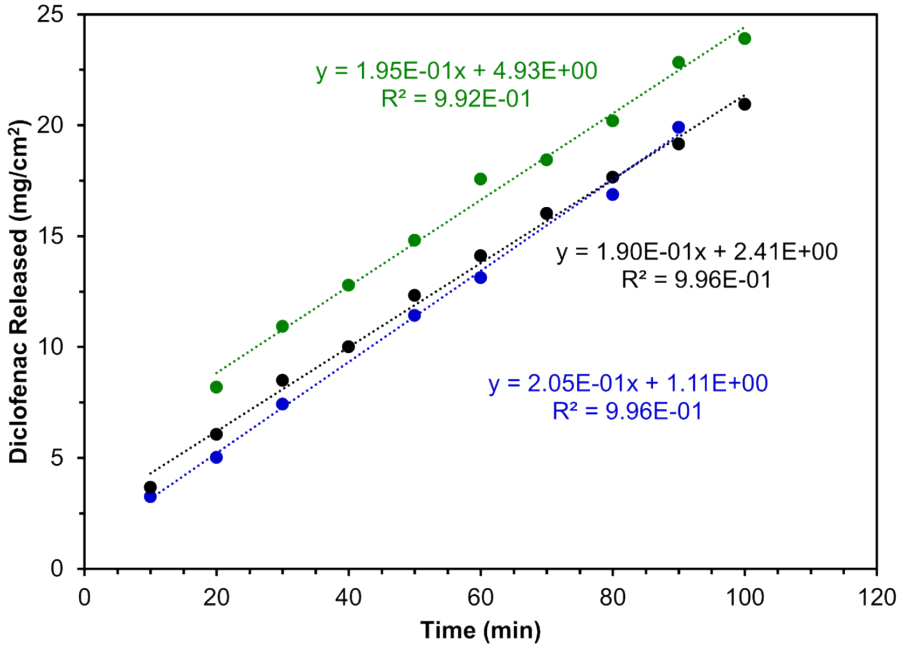

Figure S79: Intrinsic dissolution replicates of $Mg(Diclo)_2(biim\text{-}6)(EtOH)_2$ in 0.05 M phosphate buffer, pH 6.8 with 0.05% EDTA. Linear fitting of data corresponds to the intrinsic dissolution rate. Linear equation and corresponding R^2 values are shown in colors to match data sets.

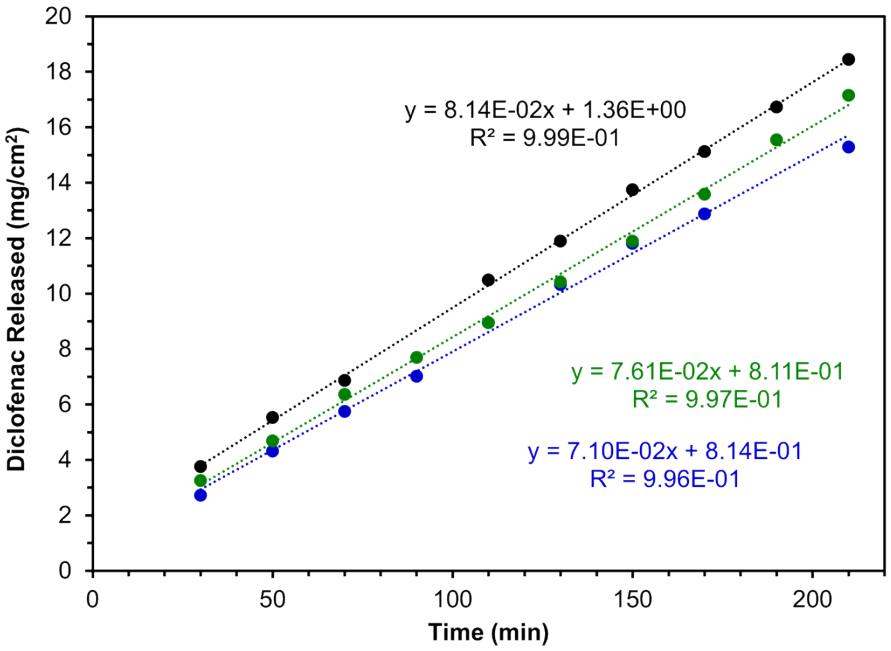

Figure S80: Intrinsic dissolution replicates of $Mn(Diclo)_2(biim\text{-}6)(EtOH)_2$ in 0.05 M phosphate buffer, pH 6.8 with 0.05% EDTA. Linear fitting of data corresponds to the intrinsic dissolution rate. Linear equation and corresponding R^2 values are shown in colors to match data sets.

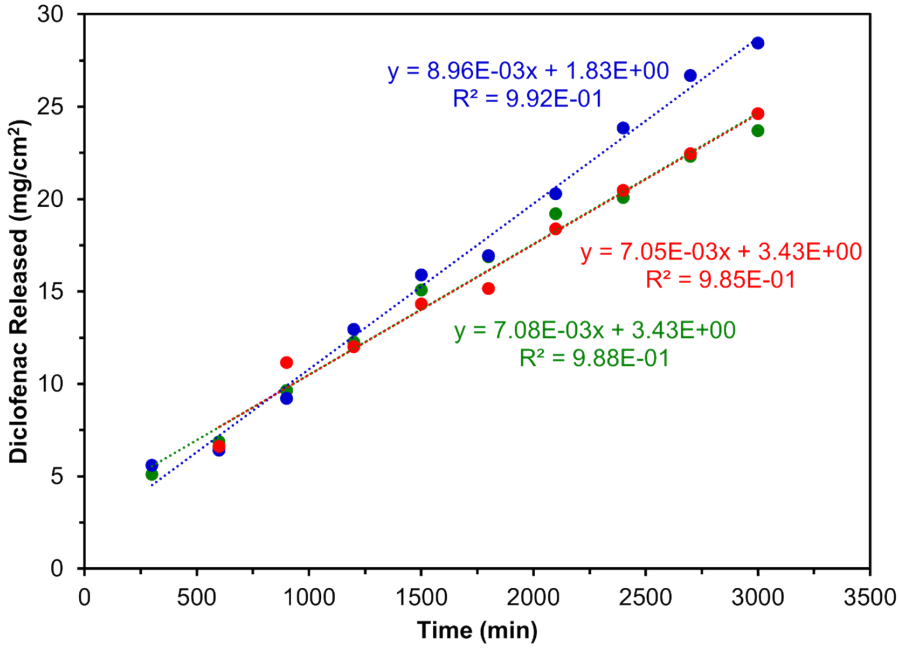

Figure S81: Intrinsic dissolution replicates of $Cu(Diclo)_2(biim\text{-}6)'$ in 0.05 M phosphate buffer, pH 6.8 with 0.05% EDTA. Linear fitting of data corresponds to the intrinsic dissolution rate. Linear equation and corresponding R^2 values are shown in colors to match data sets.

6. Scanning Electron Microscopy (SEM)

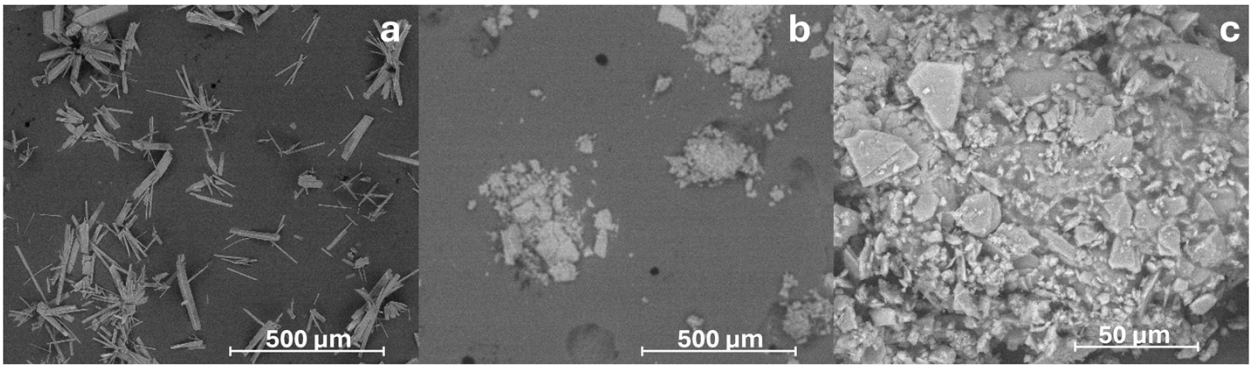

Figure S82. SEM images of $Cu(Diclo)_2(biim\text{-}6)'$ a) as-synthesized and b,c) post-grinding. The particle size distribution in images b and c range from 0.99 µm to 96.25 µm.

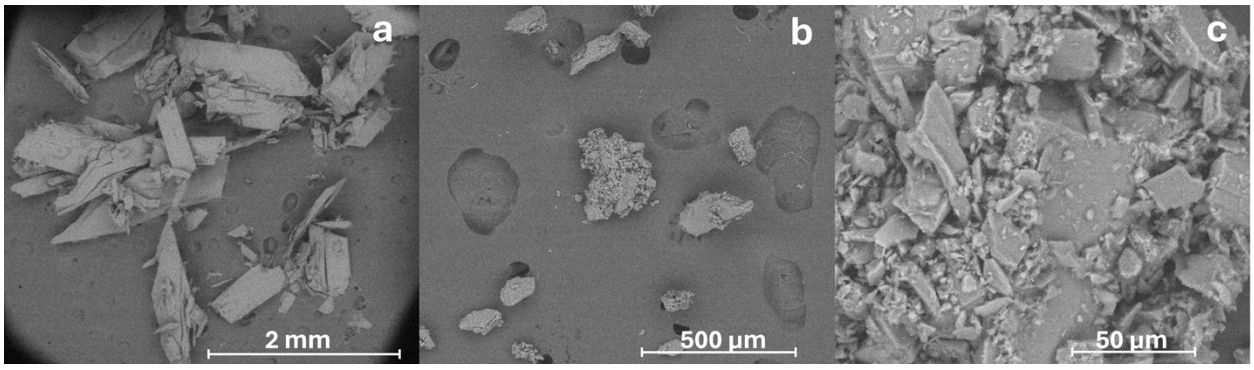

Figure S83. SEM images of $Mg(Diclo)_2(biim\text{-}6)_2(EtOH)_2$ a) as-synthesized and b,c) post-grinding. The particle size distribution of images b and c range from 1.49 µm to 389.63 µm.

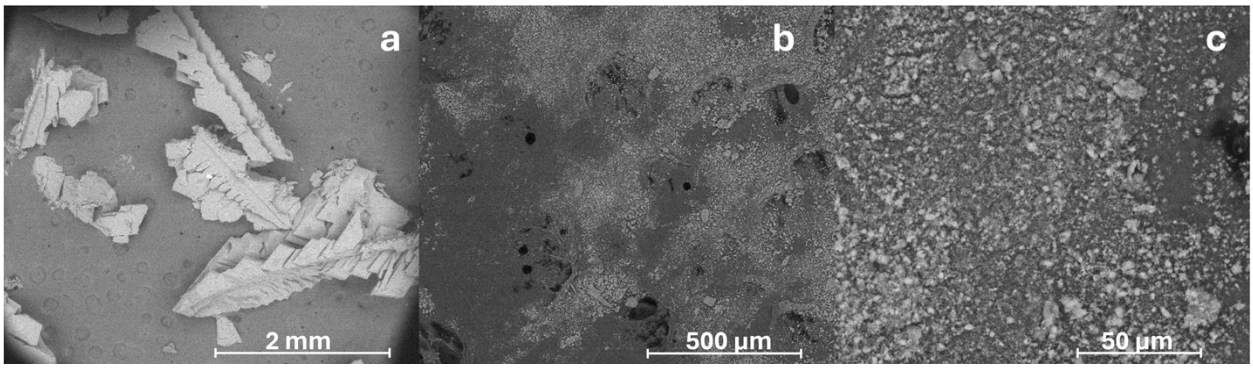

Figure S84. SEM images of $Mn(Diclo)_2(biim\text{-}6)_2(EtOH)_2$ a) as-synthesized and b,c) post-grinding. The particle size distribution in images b and c range from 0.78 µm to 14.97 µm.

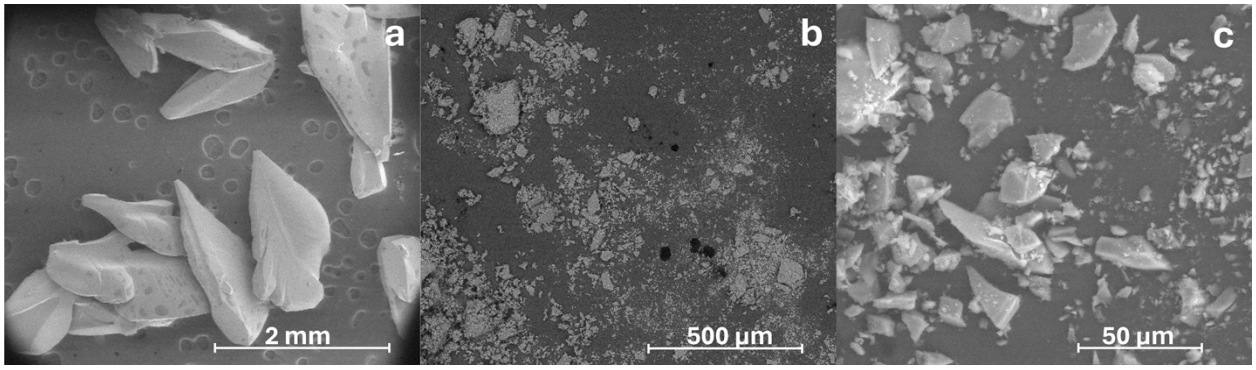

Figure S85. SEM images of $Zn(Diclo)_2(biim\text{-}6)\cdot(EtOH)$ a) as-synthesized and b,c) post-grinding. The particle size distribution in images b and c range from 0.55 µm to 193.85 µm.